# Contrasting Air Pollution Responses to Hourly Varying Anthropogenic $NO_x$ Emissions in the Contiguous United States

Madankui Tao[1,2,3*], Arlene M. Fiore[1,2], Louisa K. Emmons[4], Jeffery R. Scott[1], Gabriele G. Pfister[4], Duseong S. Jo[5], Wenfu Tang[4]

[1]Earth Atmospheric and Planetary Sciences, Massachusetts Institute of Technology, Cambridge, MA, 02139, USA,
[2]Lamont-Doherty Earth Observatory, Columbia University, Palisades, NY, 10964, USA,
[3]Department of Earth and Environmental Sciences, Columbia University, New York, NY, 10027, USA,
[4]Atmospheric Chemistry Observations & Modeling Laboratory, National Center for Atmospheric Research, Boulder, CO, 80301, USA,
[5]Department of Earth Science Education, Seoul National University, Gwanak-gu, Seoul, 08826, South Korea.

*Correspondence to*: Madankui Tao (taoma528@mit.edu)

**Abstract** (250 Word Limit)

Some global atmospheric chemistry modeling applications assume that intra-month variability in anthropogenic emissions averages out at monthly timescales. To systematically quantify the impacts of resolving daily and hourly emissions, we use a global model with a refined ~14 km resolution over the contiguous United States (CONUS; MUSICAv0) and a regional CONUS inventory for July 2018. Switching from daily to hourly nitric oxide (NO) emissions (typically higher during the day and lower at night) yields contrasting spatial responses in nitrogen oxides ($NO_x \equiv$ NO+ nitrogen dioxide ($NO_2$)) and ozone ($O_3$) concentrations in the western versus eastern CONUS and in urban versus rural areas. Neglecting hourly variations in CONUS NO emissions leads to grid-cell level monthly mean discrepancies of -49 % to +86 % (-1 to +8 ppb) for surface $NO_2$ and -22 % to +11 % (-7 to +5 ppb) for $O_3$, with tropospheric $NO_2$ columns showing similar spatial patterns (-12 % to +56 %). While comparable in magnitude to a uniform 30% NO emission reduction (grid-cell level differences of -12 % to +9 %, -7 to +3 ppb for $O_3$), the spatial response patterns differ with location-specific timing of emissions and meteorology. For example, higher morning $NO_x$ concentrations and stronger $NO_x$-saturated $O_3$ suppression occurs in Los Angeles compared to New York City. A simple scaling analysis suggests that neglecting hourly emissions variability can bias $NO_x$ emissions inferred from monthly mean tropospheric $NO_2$ columns, with absolute relative differences ranging from ~1% to ~56% within individual model grid cells.

## 1 Introduction

Exposure to ground-level ozone ($O_3$) pollution can intensify the risk of respiratory and cardiovascular diseases (Dedoussi et al., 2020; Di et al., 2017a, b; Strosnider et al., 2019). However, understanding the drivers of surface $O_3$ variations is challenging due to its formation through nonlinear photochemical reactions involving its precursors: nitrogen oxides ($NO_x$), volatile organic compounds (VOCs), and carbon monoxide (CO). Nonlinear $O_3$ production sensitivity to $NO_x$ and VOCs is

commonly described in terms of three photochemical regimes: the $NO_x$-saturated regime, in which $O_3$ concentrations increase with reductions in $NO_x$ or increases in VOCs; the $NO_x$-sensitive regime, in which $O_3$ increases with increasing $NO_x$ but shows limited response to VOCs; and a transitional regime, where $O_3$ responds similarly to changes in both precursors (Kleinman, 1994, 2005; Sillman, 2003; Sillman and He, 2002; Tonnesen and Dennis, 2000). Identifying these regimes in time and space requires diagnostic tools, and air quality models serve this role by bridging observational gaps, attributing pollution sources, and quantifying $O_3$ sensitivity to precursor emissions. Accurate anthropogenic emissions are critical for ensuring reliable model performance in these applications. We focus here on how temporal changes in emissions influence pollutant concentrations, highlighting the importance of accounting for diurnal variability when interpreting or inferring emissions from observed concentrations, and vice versa. Below, we specifically address the question: How does the temporal resolution (monthly, daily, or hourly) of anthropogenic emissions inventories affect model simulations of $O_3$ concentrations and its precursors, along with their spatiotemporal variations across the contiguous United States (CONUS)?

Recent advances in global chemistry models include the introduction of variable resolution options for continental-scale air pollution modeling (e.g., Wang et al., 2004; Goto et al., 2020; Krol et al., 2005), with studies showing that higher horizontal resolutions generally improve model alignment with observations (e.g., Schwantes et al., 2022; Jo et al., 2023; Yu et al., 2016). The variable resolution option provides high resolution over specified regions while avoiding the need for boundary conditions required by regional models, enabling studies of local-to-global influences on regional air pollution within a framework of globally consistent dynamics, physics, and chemistry. Version 0 of the Multi-Scale Infrastructure for Chemistry and Aerosols (MUSICAv0) is a configuration of the Community Atmosphere Model with chemistry (CAM-chem) and horizontal regional mesh refinement using the spectral element dynamical core (Pfister et al., 2020). Previous applications of MUSICAv0 have been used to investigate $O_3$ photochemistry in the southeast U.S. (Schwantes et al., 2022), the effects of wildfires (Tang et al., 2022, 2023b, 2025), and air quality in Africa (Tang et al., 2023a) and South Korea (Jo et al., 2023).

Global atmospheric chemistry models often do not represent daily and diurnal variations in anthropogenic emissions, instead using monthly averaged inventories, particularly as some regions lack high temporal resolution inventories and hourly emission inventories require substantial disk storage. Furthermore, their influence on simulated concentrations is not well characterized. Options exist to incorporate detailed diurnal and day-of-week variations directly in the input emissions files by providing all dates and hours, as we implement below, or by applying geographically varying scaling factors for selected regions and species (Keller et al., 2014; Lin et al., 2021). Prior regional chemical transport model (CTM) studies have examined the sensitivity of simulated surface air pollutant concentrations to sub-daily (hourly or diurnal) variations in anthropogenic emissions across a range of modeling frameworks (e.g., WRF-CMAQ, CHIMERE). These studies show that the temporal allocation of emissions can influence pollutant concentrations and their daytime-nighttime contrasts, particularly for species with strong diurnal variability such as $NO_x$ and $O_3$ (e.g., Guevara et al., 2025; Jo et al., 2023; Menut et al., 2012; Shen et al., 2023). Despite their increasing relevance for interpreting retrievals from geostationary satellite missions such as Tropospheric Emissions: Monitoring of Pollution (TEMPO), a systematic quantification of how hourly anthropogenic emissions affect daily or monthly averages of both surface and column concentrations over the United States remains lacking.

We show below that neglecting hourly variations in anthropogenic emissions can lead to discrepancies in simulated monthly mean $NO_x$ and $O_3$ concentrations, ranging from -49% to +86% for $NO_2$ and from -22% to +11% for $O_3$ within individual model grid cells, and in emissions inferred from satellite-based observations. We select July 2018 as a representative summer month for our analysis because it coincides with the availability of TROPOspheric Monitoring Instrument (TROPOMI) observations beginning in May 2018. Our summer focus reflects active photochemistry during this season, when surface $O_3$ concentrations are typically highest and most likely to exceed the U.S. National Ambient Air Quality Standards (NAAQS) (Tao et al., 2022, 2025). In this study, we evaluate MUSICAv0 simulations and examine diurnal variations in emissions and concentrations. Section 2 describes the model framework and simulation design, including the BASE simulation with a global anthropogenic emissions inventory and modifications that incorporate a regional inventory over CONUS (Section 2.1). Section 3 compares the model simulations against surface measurements of trace gases ($O_3$, $NO_2$, CO, and sulfur dioxide ($SO_2$)) and fine particulate matter ($PM_{2.5}$), as well as TROPOMI satellite retrievals of tropospheric $NO_2$ and HCHO and total column CO. After briefly describing these observational datasets (Section 3.1), we assess the impact of using the regional emissions (Section 3.2) and incorporating hourly emission variations (Section 3.3). We then examine diurnal and weekday-weekend patterns in pollutant concentrations (Section 3.4). Section 4 isolates the effects of resolving hourly nitric oxide (NO) emissions: we first examine west-to-east contrasts in surface pollutant responses (Section 4.1) and urban case studies in Los Angeles and New York City (Section 4.2), and then present a simplified analysis of the implications for constraining $NO_x$ emissions from monthly mean polar-orbiting satellite retrievals when diurnal emission variability is neglected (Section 4.3). Section 5 summarizes the key findings and discusses their implications.

## 2 Model Description and Simulations

We use a standard configuration of MUSICAv0 that features a ~14 km × 14 km refined grid for the CONUS ("ne0CONUSne30x8"), which has been shown to better represent observed surface concentrations of $O_3$ and its precursors such as $NO_x$ and CO compared to the ~100 km ("ne30") global horizontal resolution (Schwantes et al., 2022). We conduct all simulations for the year 2018. The MUSICAv0 atmospheric model is a configuration of CAM6-chem, version 6 of the Community Atmosphere Model (CAM6), which is a component of the Community Earth System Model (CESM) version 2.2 (Danabasoglu et al., 2020; Emmons et al., 2020). The CAM meteorology is nudged to the 3-hourly Modern-Era Retrospective analysis for Research and Applications Version 2 (MERRA2) meteorology (Gelaro et al., 2017). The MUSICAv0 (CESM2/CAM6-chem) model simulations use 32 vertical layers from the surface up to about 1 hPa (~45 km) (Tilmes et al., 2019).

In the standard simulation (hereafter, BASE), we use MOZART-TS1 troposphere-stratosphere chemistry (Emmons et al., 2020; Tilmes et al., 2019), with monthly Copernicus Atmosphere Monitoring Service (CAMS-GLOB-ANT) v5.1 for global anthropogenic emissions (Eskes et al., 2021) and daily Fire INventory from NCAR (National Center for Atmospheric Research) (FINN) v2.5 (Wiedinmyer et al., 2023) for biomass burning emissions. Biogenic emissions of VOCs and CO are

calculated online in the land component of CESM (Lawrence et al., 2019) based on the Model of Emissions of Gases and Aerosols from Nature (MEGAN) version 2.1 (Guenther et al., 2012). Additional emissions, such as soil $NO_x$, oceanic CO, and hydrocarbons, are taken from the POET inventory (Granier et al., 2005). Dry deposition is calculated interactively through coupled atmospheric and land models, parameterized by meteorology and biophysics (Emmons et al., 2020). We prescribe latitudinally varying fixed mixing ratio lower boundary conditions for carbon dioxide ($CO_2$), methane ($CH_4$), nitrous oxide ($N_2O$), and other well-mixed greenhouse gases, based on the ScenarioMIP SSP5-8.5 pathway from the Coupled Model Intercomparison Project Phase 6 (CMIP6) (Meinshausen et al., 2017; Montzka et al., 2004).

The BASE simulation covers the period from January to September 2018. Previous studies using CESM2.2 have employed nudging relaxation times of 50 hours (Schwantes et al., 2020), 12 hours (Tang et al., 2023b), and 6 hours (Tang et al., 2022). For the BASE simulation, we adopt an intermediate option of 12-hour nudging relaxation time as recommended for driving the model with 3-hour meteorology fields (Davis et al., 2022; Gaubert et al., 2020; Schwantes et al., 2022). Only 'T' (air temperature), 'U' (zonal wind velocity), and 'V' (meridional wind velocity) are nudged. We conduct short perturbation simulations relative to the BASE case from July 1-5, 2018 (Table S1) to test sensitivity to changes in total anthropogenic and biogenic emissions and to an alternative chemical mechanism with more detailed isoprene and terpene chemistry (Schwantes et al., 2022), providing context for interpreting the BASE case and confirming that our model setup responds consistently with previous studies (Text S1; Figs. S1 and S2). We also confirm that using 12-hour nudging maintains consistent meteorological conditions (T, U, V) across emission scenarios, ensuring that weather variability does not substantially affect conclusions drawn by differencing simulations (Text S2; Fig. S3). For simulations covering July 2018 (Table 1), we save hourly mean diagnostics of meteorological conditions, concentrations of major trace gases and aerosols, their deposition fluxes, as well as $O_3$ production and loss rates.

**Table 1: MUSICAv0 BASE configuration (January-September 2018) and U.S. Environmental Protection Agency (EPA) National Emissions Inventory (NEI) sensitivity simulations with modifications (Section 2.1) to anthropogenic emissions (July 2018). The last two columns indicate whether each simulation includes day-specific weekday-weekend and/or diurnal variability in anthropogenic emissions.**

| Simulation ID | Anthropogenic Emissions Perturbation | | |
|---|---|---|---|
| | Details | Weekday-weekend Variability | Diurnal Variability |
| **BASE** | Monthly CAMS-GLOB-ANT v5.1 anthropogenic emissions everywhere | No | No |
| **NEI_monthly** | Monthly NEI data replaces the CAMS-GLOB-ANT v5.1 anthropogenic emissions over the CONUS | No | No |
| **NEI_monthly_m30anthroNO** | Same as NEI_monthly, but anthropogenic NO emissions are reduced by 30% | No | No |

| | | | |
|---|---|---|---|
| **NEI_monthly_m30anthroVOC** | Same as NEI_monthly, but anthropogenic VOC emissions are reduced by 30% | No | No |
| **NEI_hourly** | Hourly NEI data replaces anthropogenic emissions over the CONUS | Yes | Yes |
| **NEI_hourly_NO** | Same as NEI_monthly, but with hourly NO emissions from the NEI over the CONUS | Yes (NO only) | Yes (NO only) |
| **NEI_daily_NO** | Same as NEI_monthly, but with daily-mean NO emissions from the NEI over the CONUS | Yes (NO only) | No |

### 2.1 Modifications to the CONUS Anthropogenic Emissions Inventory

To evaluate the sensitivity of simulated air pollutant concentrations to the temporal resolution of anthropogenic emissions, we use CAMS-GLOB-ANT as the global baseline inventory and replace it with the U.S. Environmental Protection Agency (EPA) National Emissions Inventory (NEI) over the CONUS, which provides more detailed (higher spatial resolution; hourly-varying) regional emissions. We then conduct a series of simulations that differ only in the temporal resolution of NEI emissions (monthly, daily, or hourly) to isolate the model response to emission timing while holding July total monthly emissions constant.

CAMS-GLOB-ANT provides monthly averages for 36 emitted compounds within 17 sectors at a spatial resolution of 0.1° × 0.1° (latitude × longitude) (Soulie et al., 2023). Here, we use CAMS-GLOB-ANT version 5.1 (Eskes et al., 2021), which combines the Emissions Database for Global Atmospheric Research (EDGAR) v5 (Crippa et al., 2019) up to 2015 with the Community Emissions Data System (CEDS) (McDuffie et al., 2020) to extrapolate emissions from 2016 to 2021. The U.S. NEI is a national inventory that includes emissions of criteria pollutants, precursors, and hazardous air pollutants (U.S. Environmental Protection Agency, 2024). The NEI is updated every three years and constructed through the Emissions Inventory System (EIS), which collects and integrates data primarily provided by State, Local, and Tribal air agencies. We first process the 2017 NEI (U.S. Environmental Protection Agency, 2022), the most recent pre-COVID inventory available at the time of this study, to hourly resolution on a ~0.1° × 0.1° grid over the CONUS (Text S3) using sector-specific diurnal profiles to capture within-day as well as day-to-day variations. The 2017 hourly NEI data are then shifted by one calendar day so that the weekday-weekend cycle matches the 2018 calendar, then re-gridded (mass-conserving) to the unstructured ne0CONUSne30x8 horizontal resolution using NCAR-developed tools (National Center for Atmospheric Research, 2022a, b). All subsequent references to NEI in this study refer to this adjusted product unless otherwise noted.

We replace CAMS-GLOB-ANT v5.1 emissions over the CONUS with these NEI products (monthly, daily, or hourly), retaining CAMS monthly means elsewhere. Switching from CAMS-GLOB-ANT v5.1 to monthly mean NEI emissions yields widespread decreases in most emitted species across the CONUS, particularly for NO and CO (Fig. S4c). Changes in anthropogenic VOC emissions are also evident (Fig. S4c), but their magnitude remains small compared with biogenic VOC

emissions (compare Fig. S5 with Fig. S4a-b; see Text S4 for the full list of emitted VOC species). The NEI products capture weekday-weekend differences in hourly and daily forms but not in monthly means. We verified that hourly NEI emissions are read by MUSICAv0 in UTC time with the prescribed diurnal and weekday-weekend variability preserved in local time at the grid-cell level (Text S3; Figs. S6 and S7).

To assess the impact of using an alternate anthropogenic emissions inventory and different temporal resolutions of emissions, we conduct four one-month simulations (Table 1): 1) monthly NEI data replace CAMS-GLOB-ANT v5.1 emissions over the CONUS, with CAMS monthly means retained elsewhere (*NEI_monthly*); 2) as in NEI_monthly except for hourly NEI emissions for all species over the CONUS (*NEI_hourly*); 3) as in NEI_monthly, but applying hourly variability only to NO emissions (*NEI_hourly_NO*); 4) as in NEI_monthly, but applying daily NO emissions with weekday-weekend differences (*NEI_daily_NO*). Here, anthropogenic $NO_x$ emissions are provided as NO, the predominant emitted form of $NO_x$. Hourly NEI emissions (NEI_hourly and NEI_hourly_NO) include day-specific diurnal variability (and therefore distinguish between weekdays and weekends), whereas NEI_daily_NO removes within-day (diurnal) variability (Table 1). The NEI_monthly vs. BASE comparison isolates the effect of changing emission inventories, NEI_hourly vs. NEI_monthly assesses the influence of adding sub-monthly (daily and diurnal) variability for all anthropogenic emissions, NEI_daily_NO vs. NEI_monthly isolates the effect of weekday-weekend differences in NO emissions, and NEI_hourly_NO vs. NEI_daily_NO isolates the effect of the diurnal changes in NO emission.

We conduct two additional one-month simulations using the NEI_monthly case as the reference to analyze the $O_3$ production regime under perturbations to anthropogenic $NO_x$ and VOC emissions. In one simulation, we reduce anthropogenic NO emissions by 30% (*NEI_monthly_m30anthroNO*) and in another we reduce anthropogenic VOC emissions by 30% (*NEI_monthly_m30anthroVOC*) (Table 1). These additional sensitivity simulations provide context for those incorporating the more nuanced changes in the temporal resolution of anthropogenic emissions (Text S4).

## 3 Evaluating the Sensitivity of Simulated Air Pollution to Emission Inventory Choice and Temporal Resolution

To account for regional variation, we divide the CONUS into six regions: West Coast, Mountain, Midwest, Southwest, Northeast, and Southeast (Fig. 1). For each region, Fig. 2 compares modeled (Section 2) and observed (Section 3.1) July mean surface concentrations of $NO_2$, $O_3$, and CO, as well as vertical column densities of tropospheric $NO_2$ and HCHO and total CO. We evaluate the model spatial representation of the observations using Spearman's rank correlation coefficient ($r_s$) and mean bias error (MBE), calculated from monthly mean values at all grid cells within the selected domain. Detailed statistics for July mean values, including root mean square error (RMSE) as well as absolute and relative differences for both MBE and RMSE, are provided in Table S2. Our primary focus is on $O_3$ and its precursors, though for completeness we include evaluations of surface $SO_2$ and $PM_{2.5}$ in Supplement Text S5, Fig. S2, and Table S3. The idealized 30% emission reduction experiment is included to provide a benchmark for the magnitude of effects associated with emission temporal resolution, while the urban

case studies are used to illustrate these effects at the local scale (e.g., a single model grid cell), where responses are most pronounced and easiest to interpret.

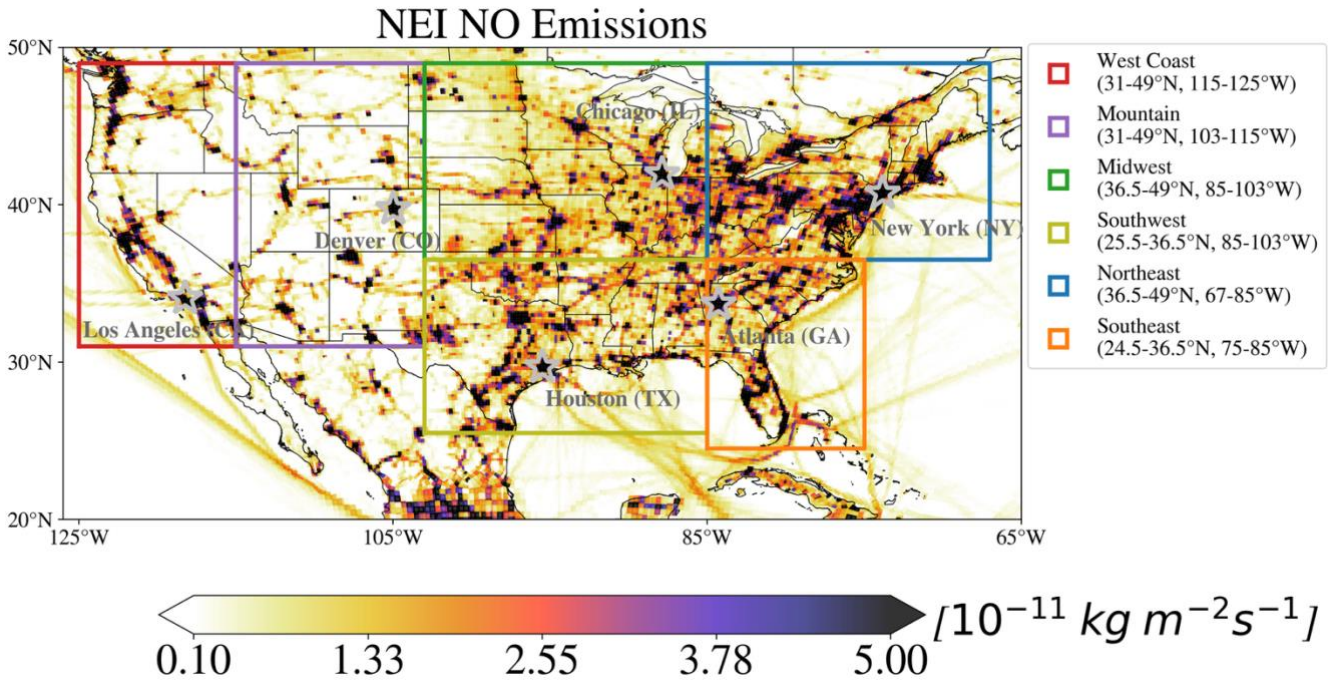


**Fig. 1: July mean nitric oxide (NO) emissions from the 2017 National Emissions Inventory adjusted to 2018, divided into six regions for model analysis: West Coast (red), Mountain (purple), Midwest (green), Southwest (yellow), Northeast (blue), and Southeast (orange). The locations of selected State and Local Monitoring Stations (SLAMS) in six major cities—Los Angeles (CA), Chicago (IL), New York City (NY), Denver (CO), Houston (TX), and Atlanta (GA)—are marked with stars.**

### 3.1 Observational Datasets for Model Evaluation

We use measurements collected from State and Local Air Monitoring Stations (SLAMS) that are reported to the U.S. EPA Air Quality System (AQS) for trace gases ($O_3$, $NO_2$, CO, and $SO_2$) and $PM_{2.5}$ concentrations (Table S4), downloaded from the AQS AirData portal (https://aqs.epa.gov/aqsweb/airdata/download_files.html; accessed August 2023). To compare MUSICAv0 surface simulations with SLAMS surface measurements, we identify the closest model grid cell based on the latitude and longitude of the SLAMS monitors. We then align hourly concentrations in local time from SLAMS with MUSICAv0 for each species across all CONUS monitors. A limitation of this evaluation is that most SLAMS sites are in urban areas and are influenced by localized effects that cannot be fully resolved by the model at 14 km resolution, which may affect the representativeness of site-level comparisons. The locations of SLAMS used in this study for each species, along with their distribution across CONUS regions and the number of monitors within selected urban grid cells, are shown in Fig. S8.

We select six monitoring stations as examples to examine diurnal patterns at individual sites (Table S5), chosen based on their proximity to major city centers across the CONUS and the availability of continuous $NO_2$ and $O_3$ measurements

throughout July 2018. Nearby stations with similar diurnal behavior were excluded to avoid redundancy. We do not average across sites as we prefer to preserve distinct local features given differences in monitor availability across cities (Fig. S8).

We also use retrievals from TROPOMI, a nadir-viewing shortwave spectrometer aboard the Sentinel 5 Precursor (S5P) satellite launched in 2017 and operational in 2018. We compare tropospheric vertical column densities ($VCD_{Trop}$) of $NO_2$ (5.5 km × 3.5 km) and HCHO (5.5 km × 3.5 km), along with total vertical column densities ($VCD_{Total}$) of CO (5.5 km × 7 km) retrieved from TROPOMI (RPRO Version 02.04.00; accessed December 2023). We select pixels with quality assurance greater than 0.75 (Table S4), which largely excludes cloudy and partly cloudy pixels (van Geffen et al., 2020; Lange et al., 2023). We re-grid the column densities and corresponding averaging kernels (AKs) to a horizontal resolution of 0.15° × 0.15°, slightly coarser than that of the model simulations over the CONUS (approximately 0.125°). TROPOMI uses *a priori* profiles derived from the TM5-MP global chemistry transport model (Myriokefalitakis et al., 2020), the massively parallel (MP) version of the Tracer Model version 5 (TM5), to simulate the vertical distribution of $NO_2$, HCHO, and CO, which are provided as supplementary data with the Level-2 products. The TM5-MP model provides data at a 1° × 1° horizontal resolution for the troposphere and upper troposphere-lower stratosphere on 34 hybrid sigma-pressure levels from the surface to approximately 0.1 hPa for retrieving the $VCD_{trop}$ of $NO_2$ and HCHO (Williams et al., 2017). The CO total column density retrievals are based on 50 hybrid sigma-pressure levels from TM5-MP.

To compare modeled column densities with TROPOMI retrievals, we mass conservatively re-grid the hourly MUSICAv0 HCHO, $NO_2$, CO, and meteorological variables to a 0.15° × 0.15° finite volume grid. We calculate the average between 1 and 2 p.m. local time (to approximate 1:30 p.m. values) for each region and apply the TROPOMI AKs, linearly interpolated vertically to the MUSICAv0 vertical resolution, to ensure a consistent application of AKs across all MUSICAv0 sensitivity simulations when calculating modeled $VCD_{Trop}$ of $NO_2$ and HCHO and $VCD_{Total}$ of CO. Our interpolation of the TROPOMI AKs to the MUSICAv0 vertical grid generally preserves their vertical structure without introducing unphysical smoothing (Fig. S9). We use the tropopause height diagnosed from the model simulations. Applying AKs to the modeled column enables a more consistent comparison between model simulations and satellite retrievals by accounting for the vertical sensitivity of the satellite instrument. We compare daily 1:30 p.m. $VCD_{trop}$ or $VCD_{Total}$ values across individual grid cells, matching each valid retrieval to the nearest model grid cell. Reported averages include only grid cells with valid retrievals.

### 3.2 Choice of Monthly Emission Inventory (BASE vs. NEI_monthly) Influences Simulated Air Pollution

Because model performance varies substantially across regions, we focus on region-specific comparisons with observations across the CONUS (Fig. 2; Tables S2 and S3), as national-level summaries may obscure important regional differences. Across the six CONUS regions, spatial correlations between observed and modeled surface concentrations in the BASE simulation (with the global CAMS-GLOB-ANT emissions) are stronger for $NO_2$ and $O_3$ ($r_s$ typically > 0.5) than for CO ($r_s$ = 0.10-0.36) (Fig. 2a; Table S2). Modeled surface concentrations of $NO_2$ are biased high by 22-40% (2-5 ppb) in all regions except the Mountain region, which shows an average low bias of 18% (1 ppb). Modeled July mean surface $O_3$ concentrations are overestimated by 11-29% (6-13 ppb). Surface CO is underestimated by 17-87% (27-140 ppb) compared to

SLAMS across all regions. Modeled July mean VCDs (Fig. 2b; Table S2) correlate spatially with TROPOMI $NO_2$ $VCD_{Trop}$ ($r_s$: 0.65-0.85) and HCHO $VCD_{Trop}$ ($r_s$ = 0.60-0.92), though the correlation is weak for CO $VCD_{Total}$ ($r_s$ = 0.11-0.53). Modeled $NO_2$ $VCD_{Trop}$ is underestimated by 34-48% (~$3\times10^{14}$ molecules/$cm^2$), while HCHO $VCD_{Trop}$ is overestimated by 15-24% (1-$4\times10^{15}$ molecules/$cm^2$) across the six regions. CO $VCD_{Total}$ is underestimated by 2-11% (3-$18\times10^{16}$ molecules/$cm^2$) in the West Coast, Midwest, and Northeast, but overestimated by 2-8% (3-$14\times10^{16}$ molecules/$cm^2$) in the Mountain, Southwest, and Southeast regions.

Compared to the BASE case, NEI_monthly (which uses monthly NEI emissions over the CONUS) improves spatial correlations ($r_s$) and reduces model biases (MBE and RMSE) for surface $NO_2$, CO, and $O_3$ concentrations, particularly in the Northeast region (Fig. 2a; Table S2). Differences in simulated surface $NO_2$ and CO between NEI_monthly and BASE (Fig. 3a) reflect emissions changes in NO and CO due to the shift from CAMS-GLOB-ANT v5.1 to NEI (Fig. S4), generally with NO reductions and CO increases despite large spatial variations, particularly over the eastern CONUS and some urban centers. Lower NEI NO emissions (Fig. S4c) reduce regional mean $NO_2$ concentrations by 1-6 ppb, bringing high biases down to within 1 ppb but exacerbating the low bias in the Mountain region to -2 ppb (Fig. 2a). CO concentrations increase relative to the BASE simulation (Fig. 3a), thus improving the surface CO underestimation by 13-55% (20-65 ppb), although low biases of 1-33% (2-71 ppb) remain (Fig. 2a). For secondary pollutants like $O_3$, changes in concentrations do not directly mirror emissions perturbations. Compared to the BASE case, surface $O_3$ concentrations decrease in NEI_monthly, except in cities with higher $NO_x$ emissions, thereby reducing modeled surface $O_3$ biases relative to SLAMS by 2-11% (approximately 1-6 ppb) across the six regional means (Figs. 2a and 3a). However, model biases of 3-21% (1-8 ppb) remain across all regions, particularly on the West Coast (NEI_monthly in Fig. 2a).

There are minimal to no changes in $r_s$ for HCHO $VCD_{Trop}$, while $NO_2$ $VCD_{Trop}$ shows weaker correlations and worsening model biases (Fig. 2b; Table S2), and changes in CO $VCD_{Total}$ exhibit large regional variability (Fig. 3b). Switching to NEI consistently decreases both surface and column $NO_2$ but not CO (Fig. 3). Compared to the BASE case, the NEI_monthly simulation worsens the model underestimates of $NO_2$ $VCD_{Trop}$ by 16-21% (~$1\times10^{14}$ molecules/$cm^2$) but decreases overestimates of regional mean HCHO $VCD_{Trop}$ by approximately 2% (0.2-$4\times10^{14}$ molecules/$cm^2$) across all regions (Fig. 2b). CO $VCD_{Total}$ shows slight increases (less than 1%) in the Southeast and slight decreases (under 2%) in other regions (Fig. 3b), with the sign of the model bias unchanged from the BASE simulation (Fig. 2b).

Biases in trace gas columns do not always match those at the surface. For instance, surface $NO_2$ shows high biases in some regions especially for the BASE simulation, while $NO_2$ $VCD_{Trop}$ are consistently biased low relative to TROPOMI (Fig. 2). These different biases in the surface versus column can arise from several factors that are independent of surface emission magnitude, including (i) vertical sensitivity and representativeness, given that satellite columns reflect vertically weighted pixel means whereas surface observations are point measurements; and (ii) retrieval uncertainties, including assumptions in the air mass factor calculation and the stratosphere-troposphere separation applied to derive tropospheric $NO_2$ columns (van Geffen et al., 2020). In addition, prior global chemistry models have been shown to underestimate background $NO_2$ $VCD_{Trop}$

relative to satellite products, partly due to uncertainties in free-tropospheric $NO_x$ chemistry and partitioning (e.g., $NO/NO_2$ ratios and partitioning among reactive nitrogen species) (van Geffen et al., 2022; Shah et al., 2023; Silvern et al., 2018, 2019).

### 3.3 Incorporating Hourly Variations in Emissions (NEI_hourly) Affects Monthly Mean Pollutant Concentrations

The surface $NO_2$ and $O_3$ concentration changes between NEI_hourly and NEI_monthly are, in some regions, similar in magnitude to those between NEI_monthly_m30anthroNO (a 30% reduction in anthropogenic NO emissions) and NEI_monthly, but the spatial patterns differ markedly (Fig. 3a), reflecting the temporal redistribution of emissions. Although overall agreement with observations changes only slightly ($r_s$, MBE, and RMSE; Fig. 2 and Tables S2 and S3), the direction and magnitude of concentration changes vary substantially across regions, especially between urban and rural areas and between the western and eastern CONUS (Figs. 3 and 4).

The largest July regional-mean difference in surface $NO_2$ (NEI_hourly − NEI_monthly) occurs on the West Coast (+16%, or +0.3 ppb), while the largest decrease is in the Northeast (-7%, -0.1 ppb) (Fig. 3a). As a result, the model shifts from underestimation to overestimation on the West Coast, while the underestimation in the Northeast becomes more pronounced for surface $NO_2$ when compared with SLAMS observations (Fig. 2a). For surface CO, changes are small and spatially varied, with regional mean increases of 2-7% (4-10 ppb) in the West Coast, Mountain, Midwest, and Southwest, and decreases of about 3% (~5 ppb) in the Northeast and Southeast (Fig. 3a). For NEI_hourly − NEI_monthly, changes in $NO_2$ $VCD_{Trop}$ and CO $VCD_{Total}$ largely mirror the surface patterns (Fig. 3b).

High model biases persist for surface $O_3$ concentrations (5-20%; 3-9 ppb) after incorporating hourly variations in emissions (NEI_hourly in Fig. 2a). Monthly mean surface $O_3$ concentrations decrease by up to ~2% (<1 ppb) in the Midwest, Northeast, and Southeast, while increases of up to ~3% (1-4 ppb) in other regions slightly worsen model overestimation. Previous studies also find model overestimates of near-surface $O_3$, with the most significant biases in the Southeast U.S., possibly reflecting uncertainties in isoprene-$NO_x$-$O_3$ chemistry, inaccuracies in dry deposition and forest canopy parameterization, and overestimates in $NO_x$ emissions (Baublitz et al., 2020; Fiore et al., 2009; Makar et al., 2017; Martin et al., 2014; Schwantes et al., 2020b; Travis et al., 2016). Although surface HCHO observations are unavailable for evaluation, modeled changes remain under 3% and follow similar spatial patterns to those of surface $O_3$ (Fig. 3a). Monthly mean HCHO $VCD_{Trop}$ decreases in the Midwest, Northeast, and Southeast but increases in other regions, mirroring the regional pattern of surface HCHO changes (Fig. 3), despite a persistent high model bias of 14-23% ($1\text{-}3\times10^{15}$ molecules/cm$^2$) (Fig. 2b; Table S2).

(a) Surface concentrations

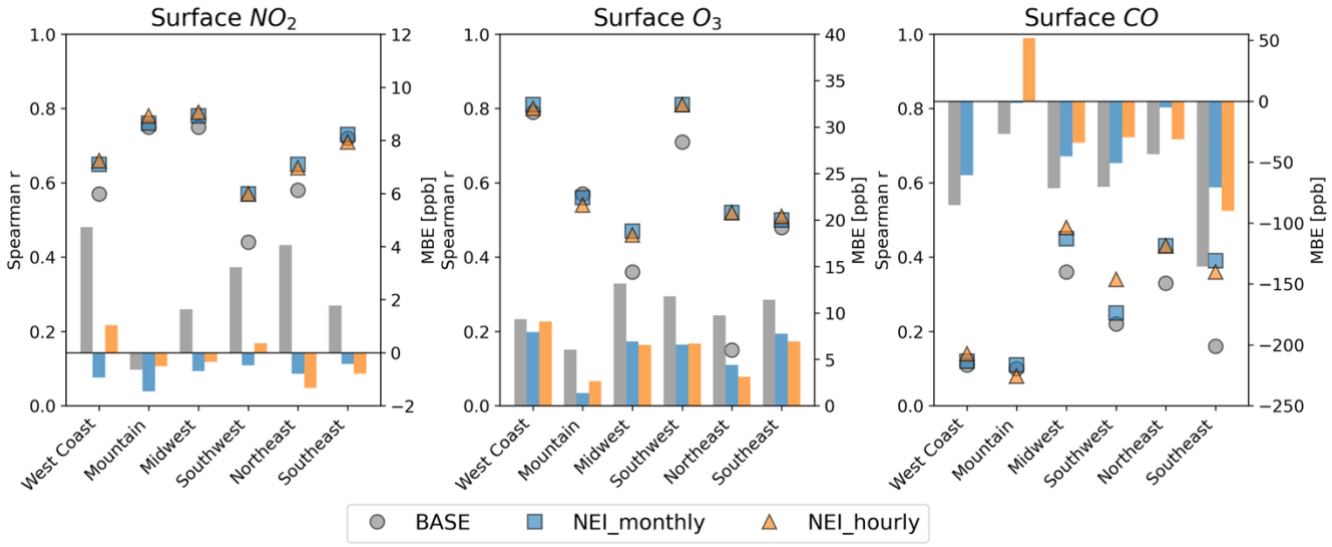


(b) Tropospheric vertical column densities ($VCD_{Trop}$)

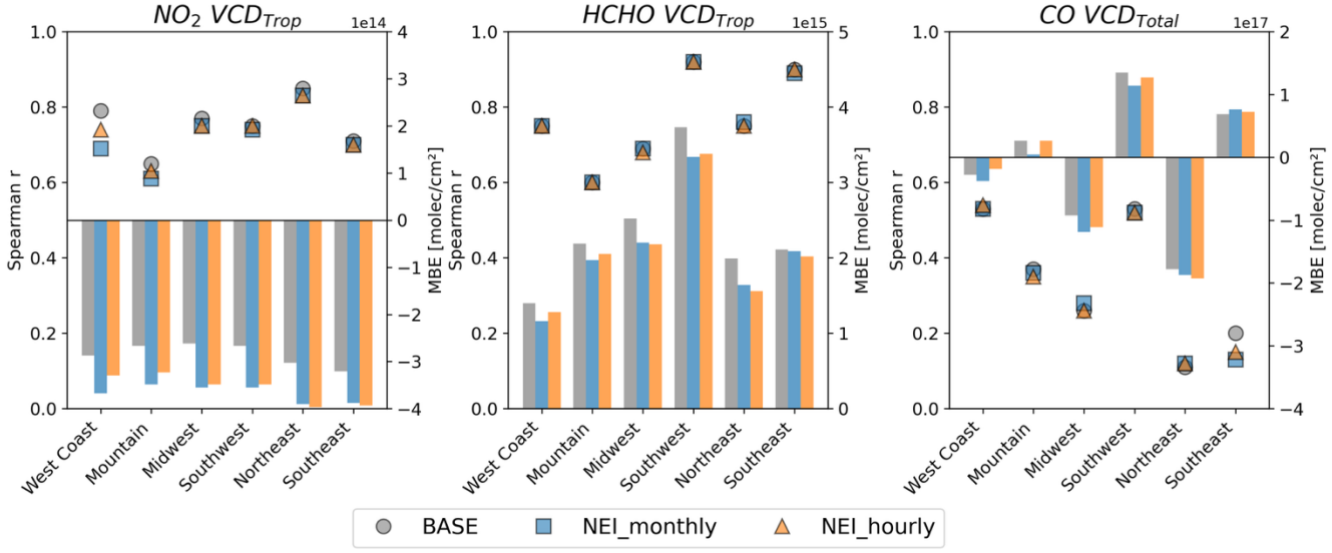


**Fig. 2: Switching to monthly NEI emissions generally improves spatial correlations and reduces biases compared with observations, whereas changes in the temporal resolution of emissions have smaller effects; both impacts differ by region. Shown are MUSICAv0-simulated (a) surface concentrations of $NO_2$, $O_3$, and CO, and (b) column densities of tropospheric $NO_2$, tropospheric HCHO, and total CO compared with observations (AQS for surface; TROPOMI for columns) for July 2018 across the six U.S. regions indicated in Fig. 1. Mean bias error (MBE; right axis) is shown as colored bars, and Spearman correlation coefficients ($r_s$; left axis) are shown as colored markers with distinct shapes. Scenarios are represented consistently across panels: BASE (gray bars/circles), NEI_monthly (blue bars/squares), and NEI_hourly (orange bars/triangles). See Table S2 for detailed statistics, including root mean square error (RMSE) and both absolute and relative differences for MBE and RMSE.**

(a) Surface concentrations

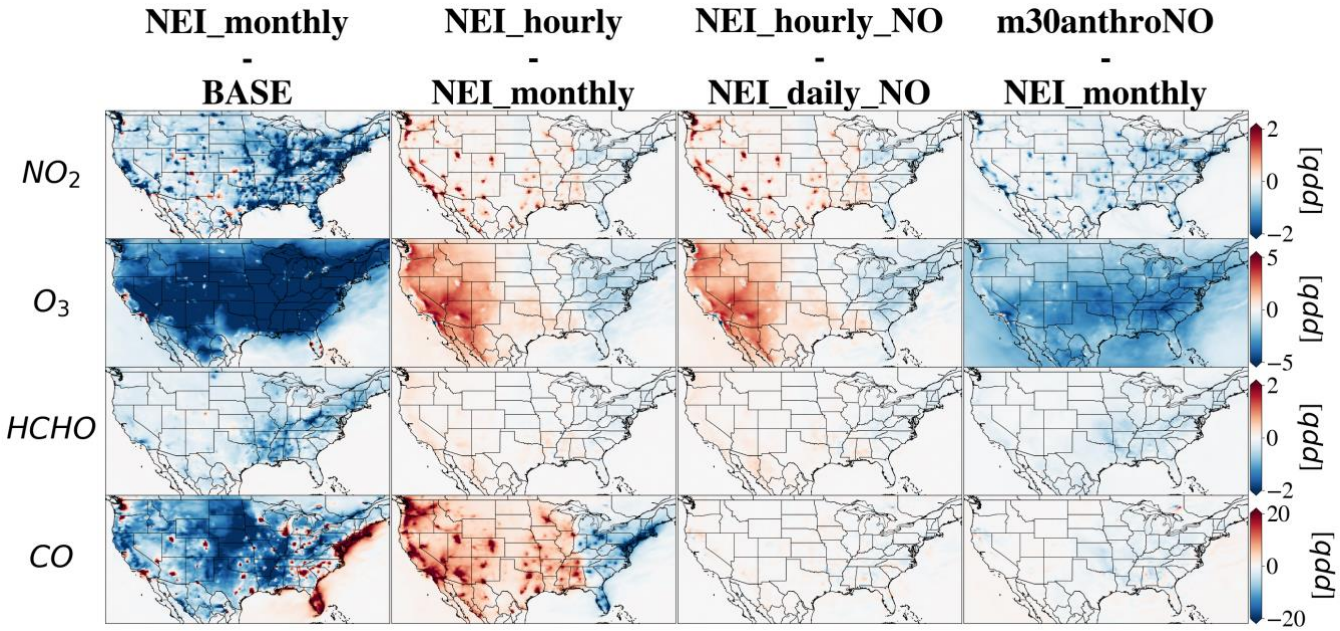


(b) Tropospheric vertical column densities ($VCD_{Trop}$)

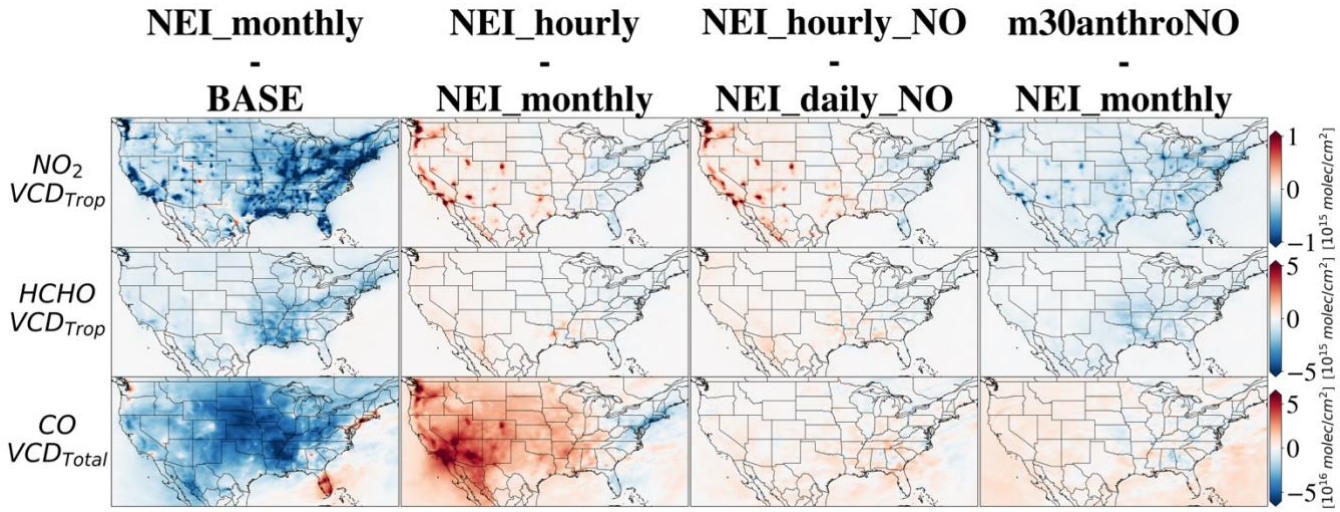


**Fig. 3: Resolving hourly variations in NO emissions produces distinct spatial responses in July monthly mean (columns; see Table 1): (a) surface concentrations, with absolute changes comparable to those from a uniform 30% reduction in monthly mean NO emissions; and (b) column densities, which generally mirror surface responses. Consistent color-bar ranges are used for each variable. See Fig. S2 for differences in surface $SO_2$ and $PM_{2.5}$.**

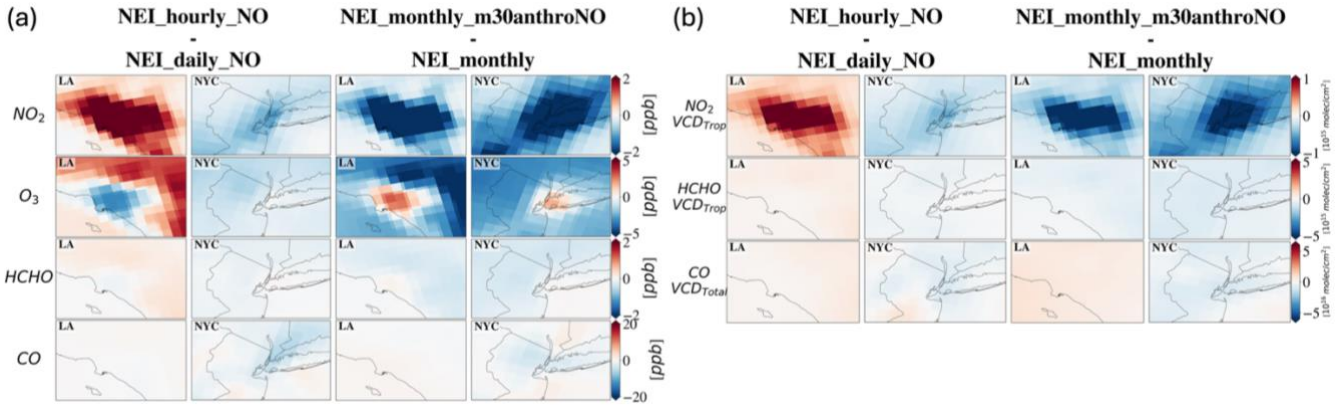


**Fig. 4: As in Fig. 3 but zoomed in over Los Angeles (LA) and New York City (NYC) and focused comparison between the responses to hourly resolved NO emissions (first two columns) versus a uniform 30% decrease in anthropogenic NO emissions (two right-most columns).**

### 3.4 Model Evaluation: Diurnal Variability and Weekday-Weekend Differences

Our model simulations (Table 1) broadly capture day-to-day variations in surface $NO_2$ and $O_3$ at the six urban sites (Fig. S10), but they tend to overestimate both the daily range and the weekday-weekend differences and misrepresent the timing of peak concentrations in most cities (Fig. S11). The exaggerated daily range largely reflects opposite model biases at different times of day: the model overestimates nighttime $NO_2$ (when concentrations are highest) and underestimates $O_3$ (at their lowest levels), while at midday it underestimates $NO_2$ and overestimates $O_3$, thereby amplifying the diurnal amplitude relative to observations (Fig S11). As expected, simulations with day-to-day variations in emissions better capture weekday-weekend concentration differences compared to NEI_monthly, though the diurnal shape still does not fully capture observations (see the right column of Fig S11). The model also misrepresents the timing of daily peaks. For example, the simulated $NO_2$ maximum occurs at 6 a.m. in Los Angeles, about two hours earlier than observed (Fig S11).

It is challenging for models to accurately represent the complex diurnal processes that shape near-surface concentrations, including boundary-layer evolution (Adams et al., 2023). Our MUSICAv0 simulations use the standard CAM6 physics configuration, including the unified Cloud Layers Unified By Binormals (CLUBB) planetary boundary layer parameterization (Bogenschutz et al., 2018; Danabasoglu et al., 2020), which has been evaluated within the CESM2/CAM6-chem framework. While the scheme generally captures the broad diurnal and seasonal structure of boundary-layer behavior, earlier work reveals overly strong nocturnal mixing and errors in the timing of the morning transition, with the direction and magnitude of these biases varying across regions and seasons (Holtslag et al., 2013; Schwantes et al., 2022; Stjern et al., 2023). Such biases may influence the simulated diurnal amplitude and timing of near-surface concentrations and their relationship to the underlying temporal profile of emissions, such as nighttime accumulation and the timing of morning concentration peaks. Errors may also arise from the NEI diurnal profiles applied in this study, which are sector-specific and derived from activity-based temporal allocation methods whose accuracy at local scales remains uncertain. In addition, comparisons between model

grid-cell means and individual SLAMS sites inevitably involve representativeness differences that may contribute to mismatches.

## 4 Sensitivity to Hourly Variations in Nitric Oxide Emissions

Imposing hourly-varying emissions results in spatially heterogeneous changes even in the monthly mean surface $NO_2$, $O_3$, and HCHO concentrations, with strong west-east and urban-rural contrasts (Figs. 3-5). We demonstrate that these simulated responses produced by switching from NEI-monthly to NEI_hourly are primarily driven by the hourly variations in NO emissions, evidenced by minimal changes between NEI_hourly_NO and NEI_hourly (<0.5% for $NO_2$, HCHO, and $O_3$). Comparisons between NEI_daily_NO and NEI_monthly, and between NEI_hourly_NO and NEI_daily_NO, indicate that these spatial patterns are shaped by switching from daily mean to hourly varying NO emissions (Figs. 3 and S12). As illustrated in Fig. 6, switching from daily mean to hourly NO emissions increases daytime and decreases nighttime emissions, with larger differences on weekdays, thereby influencing surface $NO_x$ concentrations and secondary pollutants like $O_3$.

### 4.1 West-East Contrasts in Surface Pollutant Responses

To understand the broader impacts of incorporating hourly NO emissions, we begin by examining regional contrasts in July daytime (9 a.m.-5 p.m. local time) responses across the CONUS, as shown in Fig. 5. Panel (a) maps the differences in surface NO, $NO_2$, $O_3$, and HCHO concentrations (NEI_hourly_NO minus NEI_daily_NO), while panel (b) summarizes the meridional means in 5° longitudinal bins. These plots highlight a west-to-east gradient in pollutant responses driven solely by adding the diel cycle to NO emissions. To help interpret this spatial variability, panel (c) presents the corresponding NEI_daily_NO daytime emissions and key meteorological variables, including surface temperature, planetary boundary layer height (PBLH; m above ground level), relative humidity, and $NO_2$ lifetime against dry deposition.

Polluted urban regions with higher NO emissions (Fig. 1) show more pronounced $NO_x$ concentration responses (Figs. 3 and 4). In the western CONUS, July daytime (9 a.m.-5 p.m.) monthly mean surface NO and $NO_2$ concentrations increase by up to 8 ppb and 6 ppb, respectively, in urban areas in NEI_hourly_NO simulation relative to NEI_daily_NO (Fig. 5a-b). In contrast, monthly mean daytime surface NO and $NO_2$ decrease over the eastern CONUS by up to ~1 ppb, respectively, with the largest changes also concentrated in urban areas. However, changes in surface $O_3$ do not always coincide with the largest $NO_x$ concentration changes. In the eastern CONUS, $O_3$ decreases by up to ~2 ppb (Fig. 5a-b), with the largest reductions over the polluted urban centers, consistent with prior findings (e.g., Jo et al., 2023). In contrast, monthly mean $O_3$ increases of up to 8 ppb occur over the western CONUS along the edges of —not within— urban areas (Fig. 5a). This spatial pattern points to enhanced $NO_x$ sensitivity at the periphery of $NO_x$-saturated western urban cores, consistent with our sensitivity simulations relative to the BASE case, where a 30% reduction in anthropogenic NO emissions yields the largest $O_3$ changes in surrounding rural areas (Figs. 3 and 4). In the West, the mean of the NEI_hourly_NO minus NEI_daily_NO differences exceeds the median (Fig. 5b), driven by large $NO_x$ increases in a few urban grid cells. In the East, the lower mean relative to the median reflects

strong but localized $NO_x$ decreases. By contrast, $O_3$ differences show closer agreement between mean and median across both regions, suggesting more spatially uniform impacts (Fig. 5c).

These spatial patterns are shaped by a complex interplay of background anthropogenic and biogenic emissions, local photochemical conditions, meteorology (especially boundary layer dynamics and transport), and deposition. In July, the East Coast has higher background NO emissions, approximately 70% higher over the Northeast region than over the West Coast (Fig. 1). Anthropogenic emissions across the CONUS show scattered, localized hotspots in the western U.S. and a more continuous, corridor-like pattern in the eastern U.S., consistent with population density and urban clustering (Fig. S4a). Biogenic emissions, dominated by isoprene and monoterpenes, are highest across the eastern and southern CONUS (Fig. S5). Switching to hourly emissions generally increases daytime NO (Fig. 6), yet the resulting impact on surface concentrations across the CONUS (Fig. 5a) differs notably from the response to a uniform 30% reduction in anthropogenic NO emissions (Fig. 3). This finding suggests that factors beyond total emissions, such as the timing of emissions perturbations with respect to other processes like meteorology and deposition, contribute more to the contrasting changes between the western and eastern CONUS. This contrast in $NO_x$ and $O_3$ concentration responses partly reflect systematic differences in meteorological conditions across the CONUS during July 2018 (Fig. 5c). In the eastern CONUS, shallower daytime PBLH can limit vertical mixing while enhancing both photochemical reactions and surface deposition (Y. Wu et al., 2024). Together with higher humidity in the eastern CONUS, these processes may contribute to a shorter $NO_2$ lifetime in the eastern CONUS during July 2018. We do not find evidence for a persistent east-west dipole in air stagnation, defined according to the meteorological criteria of Wang and Angell (1999).

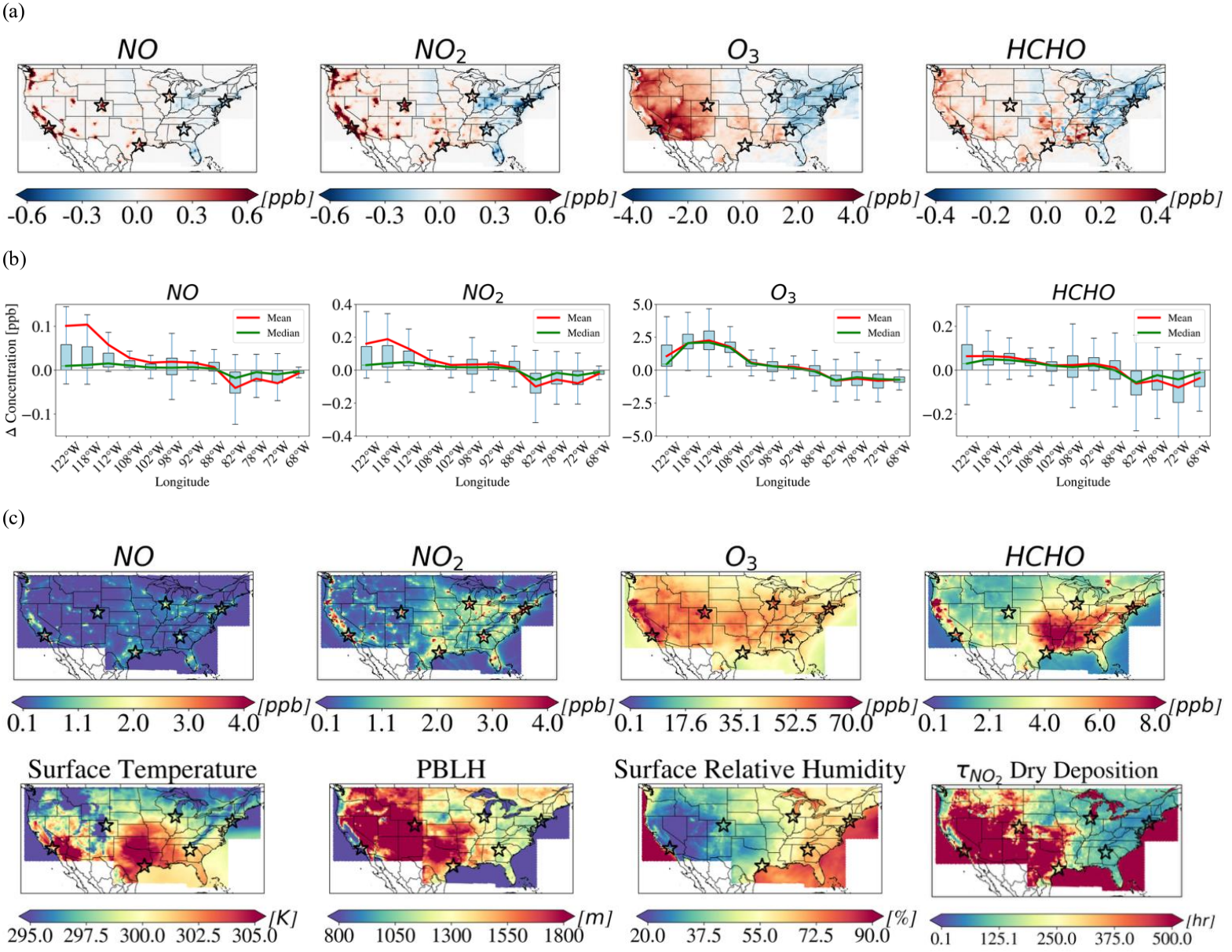
(a)
NO
NO2
O3
HCHO
-0.6 -0.3 0.0 0.3 0.6 [ppb]
-0.6 -0.3 0.0 0.3 0.6 [ppb]
-4.0 -2.0 0.0 2.0 4.0 [ppb]
-0.4 -0.2 0.0 0.2 0.4 [ppb]
(b)
NO
NO2
O3
HCHO
Mean
Median
Δ Concentration [ppb]
122°W 118°W 112°W 108°W 102°W 98°W 92°W 88°W 82°W 78°W 72°W 68°W
Longitude
(c)
NO
NO2
O3
HCHO
0.1 1.1 2.0 3.0 4.0 [ppb]
0.1 1.1 2.0 3.0 4.0 [ppb]
0.1 17.6 35.1 52.5 70.0 [ppb]
0.1 2.1 4.0 6.0 8.0 [ppb]
Surface Temperature
PBLH
Surface Relative Humidity
τNO2 Dry Deposition
295.0 297.5 300.0 302.5 305.0 [K]
800 1050 1300 1550 1800 [m]
20.0 37.5 55.0 72.5 90.0 [%]
0.1 125.1 250.0 375.0 500.0 [hr]

**Fig. 5: Resolving hourly NO emissions results in contrasting surface responses between the western and eastern CONUS and between urban and rural areas. Panel (a) shows monthly mean July daytime (9 a.m.-5 p.m. local time) differences in simulated surface concentrations of NO, $NO_2$, $O_3$, and HCHO (NEI_hourly_NO minus NEI_daily_NO). Panel (b) provides a meridional summary of the July daytime differences shown in panel (a), with values averaged within 5° longitude bins across CONUS latitudes (23-50° N). Each boxplot shows the interquartile range ($25^{th}$-$75^{th}$ percentiles) within each bin, with whiskers extending to 1.5 × interquartile range (outliers excluded); red and green lines denote the mean and median, respectively. The horizontal line marks zero change. Panel (c) displays monthly mean July daytime values from the NEI_daily_NO simulation. The first row presents surface concentrations of NO, $NO_2$, $O_3$, and HCHO, and the second row includes relevant meteorological variables: surface temperature, planetary boundary layer height (PBLH; m above ground level), and surface relative humidity. The rightmost plot in the second row shows the surface $NO_2$ lifetime against dry deposition loss.**

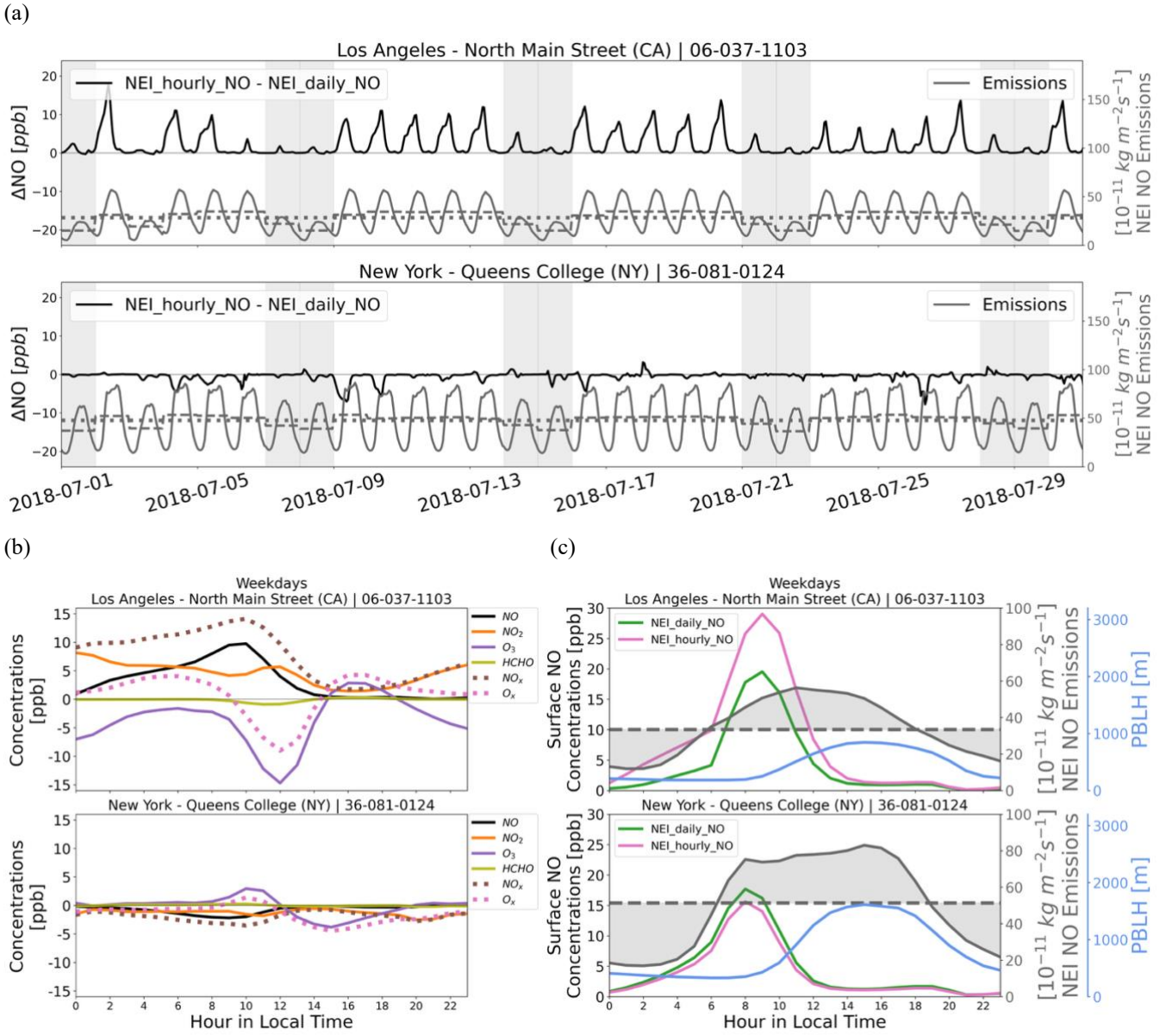


**Fig. 6: Despite similar diurnal variation in NO emissions—higher during daytime, lower at night—Los Angeles and New York City show different pollutant responses due to city-specific emission timing, boundary layer dynamics, and local photochemistry. (a) Hourly time series of July differences in surface NO concentrations between NEI_hourly_NO and NEI_daily_NO (black solid lines), alongside hourly (solid gray), daily mean (dashed), and monthly mean (dotted) NO emissions. Weekend days are shaded in gray. The lower-than-typical weekday emissions on 3 July 2018 reflect the July 4th holiday pattern in the 2017 NEI data following the shift to the 2018 calendar. Also shown are July 2018 weekday average (b) hourly surface concentration differences between NEI_hourly_NO and NEI_daily_NO for NO (black), $NO_2$ (orange) $O_3$ (purple), and HCHO (olive green), with $NO_x$ (≡ NO + $NO_2$; brown) and $O_x$ (≡ $O_3$ + $NO_2$; pink) shown as dotted lines; (c) hourly NO concentrations from NEI_daily_NO (green) and**

**NEI_hourly_NO (pink), NO emissions (gray) and PBLH (blue) for Los Angeles (top) and New York City (bottom). Solid lines represent hourly-varying emissions averaged at each hour over the month, while dashed lines indicate daily-varying emissions averaged similarly. Weekend days show similar patterns but with smaller magnitudes of change (Fig. S13). Results for all sites (including Chicago, Denver, Houston, and Atlanta; see Fig. 1), with both weekday and weekend averages shown for panels (b)-(c), are provided in Fig. S13.**

### 4.2 Urban Case Studies: Los Angeles vs. New York City

To further investigate the regional contrasts introduced in Section 4.1, we examine two representative urban centers, Los Angeles (CA) and New York City (NY), to show how local-scale meteorology and photochemistry interact with hourly NO emission patterns and result in site-specific responses in $NO_x$ and $O_3$ concentrations. Fig. 6 compares NEI_hourly_NO and NEI_daily_NO simulations, showing (a) time series of NO emissions and surface NO concentration differences, (b) July weekday-averaged diel differences in NO, $NO_2$, $O_3$, and HCHO, and (c) weekday-averaged diel cycles of NO emissions, surface NO, and PBLH. Weekend patterns are similar but generally smaller in magnitude (see Fig. S13). Fig. 7 presents July daytime $O_3$ production rates ($P(O_3)$) binned by surface $NO_x$ concentrations for the NEI_monthly, NEI_hourly_NO, and NEI_monthly_m30anthroNO simulations. Box plots summarize the distribution of $P(O_3)$ within uneven $NO_x$ concentration bins (e.g., 0-1 ppb, 1-2 ppb, ..., 5-10 ppb, 10-15 ppb, ..., >50 ppb), and color-coded points highlight values during morning, noon, and afternoon periods. Additional sites (Chicago, Denver, Houston, and Atlanta; see Fig. 1) are shown in Figs. S7, S13 and S14.

Comparing NEI_hourly_NO to NEI_daily_NO, both Los Angeles and New York City show decreases in monthly mean surface $O_3$, though with different magnitudes and opposite changes in surface $NO_x$ (Fig. 4a). Surface $NO_x$ concentrations increase in Los Angeles, especially during the morning rush-hour with boundary-layer growth, whereas they decrease in New York City (Fig. 6b-c). Surface $O_3$ decreases most in Los Angeles on weekdays between 9 a.m. and 3 p.m., outweighing a smaller late-afternoon increase (3-6 p.m.) (Fig. 6b). In New York City, the net monthly mean decrease is minimal because modest reductions from noon to evening (12-6 p.m.) only slightly exceed the morning increase (8 a.m.-12 p.m.) (Fig. 6b).

To assess $O_3$ production sensitivity to $NO_x$ and VOCs, we compare $P(O_3)$ in the 30% nationwide anthropogenic NO and VOC reduction simulations with that in NEI_monthly (Table 1). All three simulations indicate that New York City and Los Angeles are generally $NO_x$-saturated, with surface $O_3$ increasing under reduced NO emissions (Fig. 4a), whereas a 30% reduction in anthropogenic VOC emissions yields minimal changes in surface $O_3$ concentrations (<0.5% across all regions; not shown). Previous studies have shown that $O_3$ production tends to become more $NO_x$-sensitive around noon and in the afternoon, when photochemical conditions are most favorable for $O_3$ formation (Tao et al., 2022). In contrast, our results indicate that $P(O_3)$ tends to maximize during the late morning in New York City and Los Angeles, particularly under the 30% NO emission reduction scenario (Fig. 7c, f). Compared to NEI_monthly (Fig. 7a, d), reducing anthropogenic NO emissions by 30% (NEI_monthly_m30anthroNO; Fig. 7c, f) shifts the $NO_x$ concentration bins associated with high $P(O_3)$ toward lower

$NO_x$ in both Los Angeles and New York City. For example, in Los Angeles, the highest-$NO_x$ conditions (> 30 ppb) shift into lower $NO_x$ bins (< 30 ppb), bringing them closer to the $NO_x$ range associated with maximum $P(O_3)$.

Incorporating hourly NO emissions (NEI_hourly_NO) reduces July mean daytime $P(O_3)$ relative to NEI_monthly by ~2 ppb/hr in Los Angeles and ~0.3 ppb/hr in New York City. In contrast to the 30% NO reduction case (NEI_monthly_m30anthroNO), using hourly NO emissions (NEI_hourly_NO) increases the density of values in the highest $NO_x$ bins in Los Angeles, while maintaining similar $P(O_3)$ values in those bins (Fig. 7b). This extends the high-$NO_x$ tail of the $P(O_3)$-$NO_x$ distribution into more strongly $NO_x$-saturated conditions (Fig. 7b). The enhanced high-$NO_x$ tail in the NEI_hourly_NO simulation reflects larger morning $NO_x$ concentrations, when the chemical regime is most $NO_x$-saturated and $O_3$ production is suppressed. Although conditions become more $NO_x$-sensitive later in the afternoon (Fig. 7b), the larger $O_3$ decrease during late morning to early afternoon (~9-14 local time; Fig. 6b) dominates the net monthly mean $O_3$ concentration response (Fig. 4a). The more temporally concentrated (peaky) emission profile and shallower daytime PBL heights in Los Angeles compared to New York City (Fig. 6c) likely amplifies $NO_x$ accumulation, reinforcing a $NO_x$-saturated regime. Los Angeles, Denver, and Houston show broadly similar responses, while New York City, Chicago, and Atlanta exhibit distinct behavior (Figs. S13 and S14).

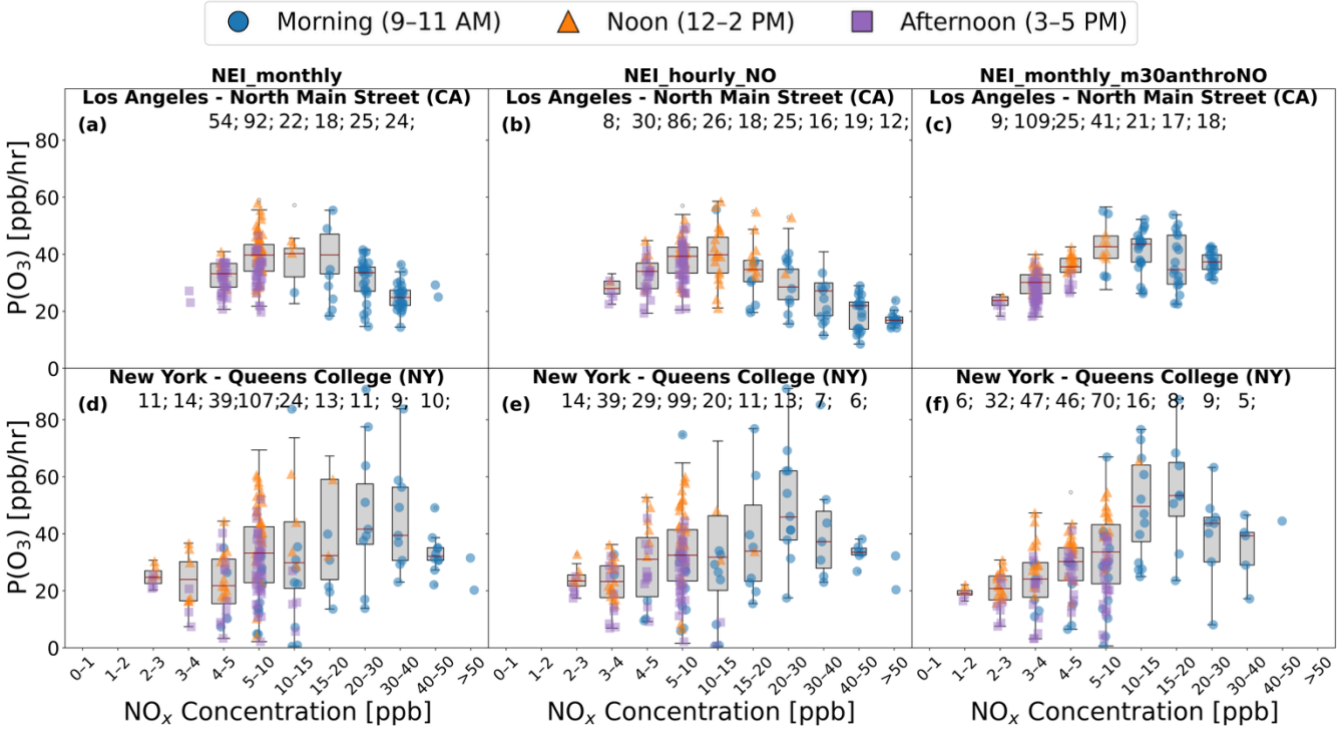


**Fig. 7: The figure shows modeled hourly $P(O_3)$ (ppb/hr) versus surface $NO_x$ concentrations (ppb) for July daytime hours (9 a.m.-5 p.m.). Columns show results for the NEI_monthly (left), NEI_hourly_NO (middle), and NEI_monthly_m30anthroNO (right) simulations. Rows show Los Angeles (CA; a-c) and New York (NY; d-f) sites. Colored points highlight local time windows: morning**

**(9-11 a.m., blue circles), noon (12-2 p.m., orange triangles), and afternoon (3-5 p.m., purple squares). Boxplots summarize the distribution of $P(O_3)$ within uneven $NO_x$ bins (e.g., 0-1 ppb, 1-2 ppb, ..., 5-10 ppb, 10-15 ppb, ..., >50 ppb) plotted at equal spacing along the x-axis. Only bins containing at least five data points are shown, and for these bins the sample size is indicated above each corresponding box: box widths scale with sample size (consistent across panels). Results for additional sites (Chicago, Denver, Houston, and Atlanta; see Fig. 1) are included in Fig. S14.**

### 4.3 Implications for Satellite-Based $NO_x$ Emission Constraints

Our results in Sections 4.1 and 4.2 show that resolving hourly NO emissions changes simulated $NO_2$ $VCD_{Trop}$ even when monthly-total emissions are the same. Given that $NO_2$ $VCD_{Trop}$ observations from satellites are commonly used to derive top-down constraints on $NO_x$ emissions (Goldberg et al., 2019; Miyazaki and Eskes, 2013), differences in emission timing representation in models used for such inversions may influence inferred emission estimates. $NO_x$ emissions are sometimes inferred using proportional scaling or mass-balance approaches, in which *a priori* emissions are adjusted based on the ratio of observed to modeled $NO_2$ columns, with chemical transport models accounting for transport and chemistry implicitly (Lamsal et al., 2011, 2014; Martin et al., 2003). More formal inverse modeling frameworks exist but similarly depend on overpass-time $NO_2$ columns and model representations of diurnal variability (Goldberg et al., 2019; Miyazaki and Eskes, 2013).

To place the magnitude of these effects in context, we perform a simple, one-month scaling-based approach for July 2018 to estimate potential biases in inferred NO emission magnitude arising from the representation of diurnal emission timing in models (details in Text S6). In this section, $\Omega$ denotes $NO_2$ $VCD_{Trop}$ and $E$ anthropogenic NO emissions. We use this illustrative simple framework but emphasize that $\Omega$ generally reflect emissions from multiple model grid cells given the $NO_x$ lifetime and transport timescales. Transport, chemistry, and lifetime effects are implicitly accounted for through the forward model but are not explicitly inverted. Accordingly, $(\Delta E/E)_{est}$ in Fig. 8 should be interpreted as an estimate of the potential bias in inferred emission magnitude rather than as a quantitative emission inversion. Using NEI_hourly_NO and NEI_monthly to isolate the effect of NO emission timing alone, with July mean $\Omega$ and identical monthly-integrated emissions, the inferred timing-representation bias is small on average over the CONUS (+1.8%) but spatially variable, with regional mean values of 1-8% in the western U.S. and approximately -3 to -2 % in the Northeast and Southeast (Fig. 8; Table S6). City-scale values are larger, reaching +26% in Los Angeles, +30% in Denver and -7% in New York City (Table S6).

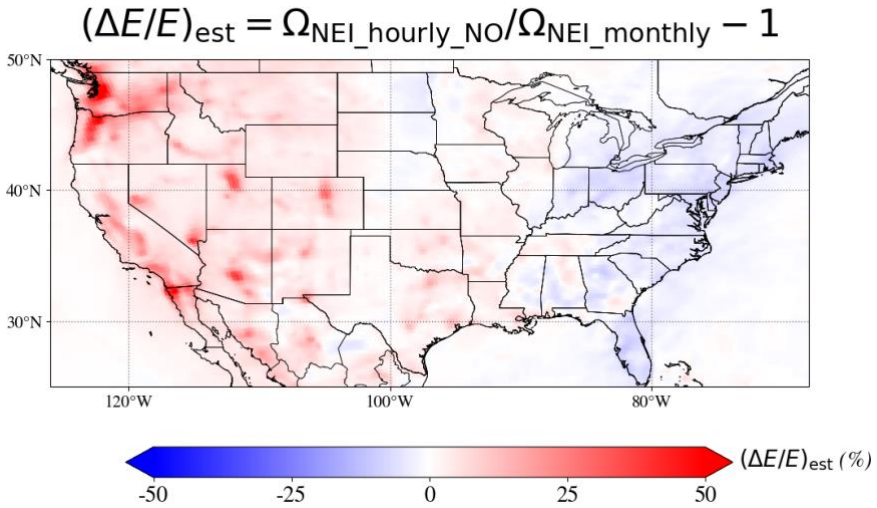


**Fig. 8: Estimated biases ($(\Delta E/E)_{est}$) in July 2018 anthropogenic NO emissions magnitude ($E$) using model-simulated tropospheric $NO_2$ columns ($\Omega$). The figure maps the potential biases resulting from neglecting hourly NO emissions, estimated by comparing July-mean $\Omega$ simulated in NEI_hourly_NO and NEI_monthly. Values are shown as percentages. Regional and city-scale statistics are provided in Table S6, with methodological details in Text S6.**

## 5 Discussion and Conclusions

We demonstrated that incorporating hourly variations in NO emissions produces substantial changes in $NO_x$ and $O_3$ concentrations, even in monthly averages, comparable in magnitude to those associated with an idealized 30% reduction in NO emissions (Figs. 3 and 4). These changes, however, are nuanced, differing between urban and rural areas and between the eastern and western U.S., reflecting region-specific emission patterns, photochemistry, and meteorological conditions (Fig. 5). Monthly mean daytime surface $O_3$ concentrations over the CONUS in July differ by up to 7 ppb (11% for NEI_hourly relative to NEI_monthly; Fig. 5), large enough to affect model-based conclusions regarding regional attainment of the U.S. NAAQS for $O_3$. In the western CONUS, monthly mean surface $NO_2$ increases by up to ~6 ppb during the daytime. In contrast, the eastern CONUS with its higher NO and biogenic VOC emissions, larger dry deposition flux rates, more humid conditions, and shallower PBLH—all of which favor a shorter $NO_2$ lifetime—experiences daytime $NO_2$ decreases of up to ~1 ppb (Fig. 5). We also find differences in $O_3$ production regimes across cities: for example, a shift toward more $NO_x$-saturated conditions in Los Angeles but toward stronger $NO_x$ sensitivity in New York City when hourly variations in NO emissions are included (Figs. 6 and 7). Spatial changes in simulated VCD closely follow those in surface concentrations (Figs. 3 and 4). Using a simple scaling-based analysis, we show that model representations of emission timing can substantially affect NO emission magnitudes estimated from satellite-retrieved $NO_2$ $VCD_{Trop}$. For July 2018, neglecting hourly variability in anthropogenic NO emissions leads to spatially heterogeneous biases in estimated emissions that are generally modest at the regional scale (a few

percent) but substantially larger at the grid-cell level, with absolute relative differences ranging from ~1% to >50% and locally reaching approximately -12% to +56% (Fig. 8).

With the advent of geostationary satellite observations, the TEMPO mission now provides continuous daytime measurements of trace gases over North America (Naeger et al., 2021; Zoogman et al., 2017). Similar geostationary retrievals have been available over East Asia since 2020 from the Geostationary Environment Monitoring Spectrometer (GEMS), with recent studies demonstrating its capability to capture diurnal variations in $NO_2$ $VCD_{Trop}$ (Edwards et al., 2024; Park et al., 2025; Yang et al., 2023). Our results demonstrate that neglecting hourly variations in emissions introduces biases when interpreting monthly mean concentrations from once-daily polar-orbiting satellite overpasses, potentially aliasing sub-daily emission variability into top-down $NO_x$ emission estimates. Emerging geostationary observations now make it possible to evaluate these intra-day effects directly to refine constraints on emission timing and related photochemical processes.

Although our analysis focuses on July 2018, the differences we identify due to the temporal resolution of emissions are broadly relevant, though their local magnitude will vary across years with both emissions and meteorology. Recent trends since 2018 could all modulate the magnitude of these effects: continued declines in anthropogenic $NO_x$ emissions (Christiansen et al., 2024); increases in temperature-sensitive soil $NO_x$ and biogenic VOCs (Geddes et al., 2022); more frequent heat waves and stagnation events (Gao et al., 2023); and episodic wildfires (Abatzoglou et al., 2025). Lower $NO_x$ emissions and flatter diurnal shapes would likely reduce the differences between using hourly and daily or monthly mean emissions, whereas more stagnant conditions could amplify $O_3$ sensitivity to the timing of precursor emissions through enhanced localized photochemical activity. While we analyzed diurnal emission cycles within the CONUS during summer, similar sensitivities are likely to occur in source regions elsewhere, underscoring the need to better characterize diurnal emission cycles and the corresponding chemical responses of air pollutants in other seasons and world regions.

**Acknowledgements**

We thank Dr. Joshua Laughner and an anonymous reviewer for their thoughtful and constructive reviews.

**Code and Data Availability**

The Multi-Scale Infrastructure for Chemistry and Aerosols version 0 (MUSICAv0) is a publicly available community model maintained by the National Center for Atmospheric Research (NCAR). Source code and documentation can be accessed at: https://www2.acom.ucar.edu/sections/MUSICA. Simulation output used in this study has been archived and is available from the corresponding author upon request. Measurements from the State and Local Air Monitoring Stations (SLAMS) network are archived and publicly available through the U.S. Environmental Protection Agency (EPA) Air Quality System Pre-Generated Data Files (U.S. Environmental Protection Agency, 2023). TROPOspheric Monitoring Instrument (TROPOMI) Level-2 products are available from the NASA Goddard Earth Sciences Data and Information Services Center (GES DISC) for formaldehyde (Copernicus Sentinel-5P, 2018a) and nitrogen dioxide (Copernicus Sentinel-5P, 2018b).

**Author contribution**

MT set up the model simulations, performed the data analysis, and wrote the manuscript. AMF provided guidance on scientific direction and simulation design, advised throughout the project, and contributed to manuscript revisions. LKE advised on the use of the MUSICAv0 model and provided technical guidance. JRS supported the CESM simulations on high-performance computing (HPC) systems. GGP processed the NEI emissions. DSJ advised on preparing emissions for the variable-resolution grid. All co-authors provided comments and suggestions to improve the manuscript.

**Competing Interests**

The authors declare that they have no conflict of interest.

**Financial Support**

This research has been supported by the National Aeronautics and Space Administration (NASA, Health and Air Quality Applied Sciences Team, HAQAST; award no. 80NSSC21K0509) and the National Science Foundation (NSF, award no. 2228379). The computations presented here were conducted using the "Svante" cluster, a facility located at MIT's Massachusetts Green High Performance Computing Center and supported by the Center for Sustainability Science and Strategy (https://cs3.mit.edu).

**References**

Abatzoglou, J. T., Kolden, C. A., Cullen, A. C., Sadegh, M., Williams, E. L., Turco, M., and Jones, M. W.: Climate Change Has Increased the Odds of Extreme Regional Forest Fire Years Globally, Nat. Commun., 16, 6390, https://doi.org/10.1038/s41467-025-61608-1, 2025.

Adams, T. J., Geddes, J. A., and Lind, E. S.: New Insights Into the Role of Atmospheric Transport and Mixing on Column and Surface Concentrations of $NO_2$ at a Coastal Urban Site, Journal of Geophysical Research: Atmospheres, 128, e2022JD038237, https://doi.org/https://doi.org/10.1029/2022JD038237, 2023.

Baublitz, C. B., Fiore, A. M., Clifton, O. E., Mao, J., Li, J., Correa, G., Westervelt, D. M., Horowitz, L. W., Paulot, F., and Williams, A. P.: Sensitivity of Tropospheric Ozone Over the Southeast USA to Dry Deposition, Geophys. Res. Lett., 47, e2020GL087158, https://doi.org/https://doi.org/10.1029/2020GL087158, 2020.

Bogenschutz, P. A., Gettelman, A., Hannay, C., Larson, V. E., Neale, R. B., Craig, C., and Chen, C.-C.: The Path to CAM6: Coupled Simulations with CAM5.4 and CAM5.5, Geosci. Model Dev., 11, 235–255, https://doi.org/10.5194/gmd-11-235-2018, 2018.

Christiansen, A., Mickley, L. J., and Hu, L.: Constraining Long-Term $NO_x$ Emissions Over the United States and Europe Using Nitrate Wet Deposition Monitoring Networks, Atmos. Chem. Phys., 24, 4569–4589, https://doi.org/10.5194/acp-24-4569-2024, 2024.

Crippa, M., Oreggioni, G., Guizzardi, D., Muntean, M., Schaaf, E., Lo Vullo, E., Solazzo, E., Monforti-Ferrario, F., Olivier, J., and Vignati, E.: Fossil $CO_2$ and GHG Emissions of All World Countries, Publications Office of the European Union, Luxembourg (Luxembourg), https://doi.org/10.2760/687800 (online),10.2760/655913 (print), 2019.

Danabasoglu, G., Lamarque, J.-F., Bacmeister, J., Bailey, D. A., DuVivier, A. K., Edwards, J., Emmons, L. K., Fasullo, J., Garcia, R., Gettelman, A., Hannay, C., Holland, M. M., Large, W. G., Lauritzen, P. H., Lawrence, D. M., Lenaerts, J. T. M., Lindsay, K., Lipscomb, W. H., Mills, M. J., Neale, R., Oleson, K. W., Otto-Bliesner, B., Phillips, A. S., Sacks, W., Tilmes, S., van Kampenhout, L., Vertenstein, M., Bertini, A., Dennis, J., Deser, C., Fischer, C., Fox-Kemper, B., Kay, J. E., Kinnison, D., Kushner, P. J., Larson, V. E., Long, M. C., Mickelson, S., Moore, J. K.,

Nienhouse, E., Polvani, L., Rasch, P. J., and Strand, W. G.: The Community Earth System Model Version 2 (CESM2), J. Adv. Model. Earth Syst., 12, e2019MS001916, https://doi.org/https://doi.org/10.1029/2019MS001916, 2020.

Davis, N. A., Callaghan, P., Simpson, I. R., and Tilmes, S.: Specified Dynamics Scheme Impacts on Wave-Mean Flow Dynamics, Convection, and Tracer Transport in CESM2 (WACCM6), Atmos. Chem. Phys., 22, 197–214, https://doi.org/10.5194/acp-22-197-2022, 2022.

Dedoussi, I. C., Eastham, S. D., Monier, E., and Barrett, S. R. H.: Premature Mortality Related to United States Cross-State Air Pollution, Nature, 578, 261–265, https://doi.org/10.1038/s41586-020-1983-8, 2020.

Di, Q., Wang, Y., Zanobetti, A., Wang, Y., Koutrakis, P., Choirat, C., Dominici, F., and Schwartz, J. D.: Air Pollution and Mortality in the Medicare Population, New England Journal of Medicine, 376, 2513–2522, https://doi.org/10.1056/NEJMoa1702747, 2017a.

Di, Q., Dai, L., Wang, Y., Zanobetti, A., Choirat, C., Schwartz, J. D., and Dominici, F.: Association of Short-term Exposure to Air Pollution With Mortality in Older Adults, JAMA, 318, 2446–2456, https://doi.org/10.1001/jama.2017.17923, 2017b.

Doherty, R. M., Wild, O., Shindell, D. T., Zeng, G., MacKenzie, I. A., Collins, W. J., Fiore, A. M., Stevenson, D. S., Dentener, F. J., Schultz, M. G., Hess, P., Derwent, R. G., and Keating, T. J.: Impacts of Climate Change on Surface Ozone and Intercontinental Ozone Pollution: A Multi-Model Study, Journal of Geophysical Research: Atmospheres, 118, 3744–3763, https://doi.org/https://doi.org/10.1002/jgrd.50266, 2013.

Edwards, D. P., Martínez-Alonso, S., Jo, D. S., Ortega, I., Emmons, L. K., Orlando, J. J., Worden, H. M., Kim, J., Lee, H., Park, J., and Hong, H.: Quantifying the Diurnal Variation in Atmospheric $NO_2$ from Geostationary Environment Monitoring Spectrometer (GEMS) Observations, Atmos. Chem. Phys., 24, 8943–8961, https://doi.org/10.5194/acp-24-8943-2024, 2024.

Emmons, L. K., Schwantes, R. H., Orlando, J. J., Tyndall, G., Kinnison, D., Lamarque, J. F., Marsh, D., Mills, M. J., Tilmes, S., Bardeen, C., Buchholz, R. R., Conley, A., Gettelman, A., Garcia, R., Simpson, I., Blake, D. R., Meinardi, S., and Pétron, G.: The Chemistry Mechanism in the Community Earth System Model Version 2 (CESM2), J. Adv. Model. Earth Syst., 12, 1–21, https://doi.org/10.1029/2019MS001882, 2020.

Eskes, H. J., Basart, S., Benedictow, A., Bennouna, Y., Blechschmidt, A.-M., Chabrillat, S., Christophe, Y., Cuevas, E., Flentje, H., Hansen, K. M., Kapsomenakis, J., Langerock, B., Ramonet, M., Richter, A., Schulz, M., Sudarchikova, N., Wagner, A., Warneke, T., and Zerefos, C.: Observation characterisation and validation methods document, Copernicus Atmosphere Monitoring Service (CAMS) report, CAMS84_2018SC2_D6.1.1-2020_observations_v5.pdf, https://doi.org/10.24380/7cjp-dn95, 2021.

Fiore, A. M., Jacob, D. J., Bey, I., Yantosca, R. M., Field, B. D., Fusco, A. C., and Wilkinson, J. G.: Background Ozone Over the United States in Summer: Origin, Trend, and Contribution to Pollution Episodes, Journal of Geophysical Research Atmospheres, 107, 2002.

Fiore, A. M., Dentener, F. J., Wild, O., Cuvelier, C., Schultz, M. G., Hess, P., Textor, C., Schulz, M., Doherty, R. M., Horowitz, L. W., MacKenzie, I. A., Sanderson, M. G., Shindell, D. T., Stevenson, D. S., Szopa, S., Van Dingenen, R., Zeng, G., Atherton, C., Bergmann, D., Bey, I., Carmichael, G., Collins, W. J., Duncan, B. N., Faluvegi, G., Folberth, G., Gauss, M., Gong, S., Hauglustaine, D., Holloway, T., Isaksen, I. S. A., Jacob, D. J., Jonson, J. E., Kaminski, J. W., Keating, T. J., Lupu, A., Marmer, E., Montanaro, V., Park, R. J., Pitari, G., Pringle, K. J., Pyle, J. A., Schroeder, S., Vivanco, M. G., Wind, P., Wojcik, G., Wu, S., and Zuber, A.: Multimodel Estimates of Intercontinental Source-Receptor Relationships for Ozone Pollution, Journal of Geophysical Research: Atmospheres, 114, https://doi.org/https://doi.org/10.1029/2008JD010816, 2009.

Gao, Y., Wu, Y., Guo, X., Kou, W., Zhang, S., Leung, L. R., Chen, X., Lu, J., Diffenbaugh, N. S., Horton, D. E., Yao, X., Gao, H., and Wu, L.: More Frequent and Persistent Heatwaves Due To Increased Temperature Skewness Projected by a High-Resolution Earth System Model, Geophys. Res. Lett., 50, e2023GL105840, https://doi.org/https://doi.org/10.1029/2023GL105840, 2023.

Gaubert, B., Emmons, L. K., Raeder, K., Tilmes, S., Miyazaki, K., Arellano Jr., A. F., Elguindi, N., Granier, C., Tang, W., Barré, J., Worden, H. M., Buchholz, R. R., Edwards, D. P., Franke, P., Anderson, J. L., Saunois, M., Schroeder, J., Woo, J.-H., Simpson, I. J., Blake, D. R., Meinardi, S., Wennberg, P. O., Crounse, J., Teng, A., Kim, M., Dickerson, R. R., He, H., Ren, X., Pusede, S. E., and Diskin, G. S.: Correcting Model Biases of CO in East Asia: Impact on

Oxidant Distributions During Korus-Aq KORUS-AQ, Atmos. Chem. Phys., 20, 14617–14647, https://doi.org/10.5194/acp-20-14617-2020, 2020.

Geddes, J. A., Pusede, S. E., and Wong, A. Y. H.: Changes in the Relative Importance of Biogenic Isoprene and Soil $NO_x$ Emissions on Ozone Concentrations in Nonattainment Areas of the United States, Journal of Geophysical Research: Atmospheres, 127, e2021JD036361, https://doi.org/https://doi.org/10.1029/2021JD036361, 2022.

van Geffen, J., Boersma, K. F., Eskes, H., Sneep, M., ter Linden, M., Zara, M., and Veefkind, J. P.: S5P TROPOMI $NO_2$ Slant Column Retrieval: Method, Stability, Uncertainties and Comparisons With OMI, Atmos. Meas. Tech., 13, 1315–1335, https://doi.org/10.5194/amt-13-1315-2020, 2020.

van Geffen, J., Eskes, H., Compernolle, S., Pinardi, G., Verhoelst, T., Lambert, J.-C., Sneep, M., ter Linden, M., Ludewig, A., Boersma, K. F., and Veefkind, J. P.: Sentinel-5P TROPOMI $NO_2$ Retrieval: Impact of Version v2.2 Improvements and Comparisons With OMI and Ground-Based Data, Atmos. Meas. Tech., 15, 2037–2060, https://doi.org/10.5194/amt-15-2037-2022, 2022.

Gelaro, R., McCarty, W., Suárez, M. J., Todling, R., Molod, A., Takacs, L., Randles, C. A., Darmenov, A., Bosilovich, M. G., Reichle, R., Wargan, K., Coy, L., Cullather, R., Draper, C., Akella, S., Buchard, V., Conaty, A., da Silva, A. M., Gu, W., Kim, G. K., Koster, R., Lucchesi, R., Merkova, D., Nielsen, J. E., Partyka, G., Pawson, S., Putman, W., Rienecker, M., Schubert, S. D., Sienkiewicz, M., and Zhao, B.: The modern-era retrospective analysis for research and applications, version 2 (MERRA-2), J. Clim., 30, 5419–5454, https://doi.org/10.1175/JCLI-D-16-0758.1, 2017.

Goldberg, D. L., Saide, P. E., Lamsal, L. N., De Foy, B., Lu, Z., Woo, J. H., Kim, Y., Kim, J., Gao, M., Carmichael, G., and Streets, D. G.: A Top-Down Assessment Using OMI $NO_2$ Suggests an Underestimate in the $NO_x$ Emissions Inventory in Seoul, South Korea, During KORUS-AQ, Atmos. Chem. Phys., 19, 1801–1818, https://doi.org/10.5194/acp-19-1801-2019, 2019.

Goto, D., Sato, Y., Yashiro, H., Suzuki, K., Oikawa, E., Kudo, R., Nagao, T. M., and Nakajima, T.: Global Aerosol Simulations Using NICAM.16 on a 14km Grid Spacing for A Climate Study: Improved and Remaining Issues Relative to a Lower-Resolution Model, Geosci. Model Dev., 13, 3731–3768, https://doi.org/10.5194/gmd-13-3731-2020, 2020.

Granier, C. , Lamarque, J. F. , Mieville, A. , Muller, J. F. , Olivier, J. , Orlando, J. , Peters, J. , Petron, G. , Tyndall, G. , and Wallens, S.: POET, A Database of Surface Emissions of Ozone Precursors, 2005.

Guenther, A. B., Jiang, X., Heald, C. L., Sakulyanontvittaya, T., Duhl, T., Emmons, L. K., and Wang, X.: The Model of Emissions of Gases and Aerosols from Nature version 2.1 (MEGAN2.1): an extended and updated framework for modeling biogenic emissions, Geosci. Model Dev., 5, 1471–1492, https://doi.org/10.5194/gmd-5-1471-2012, 2012.

Guevara, M., Colette, A., Guion, A., Petiot, V., Adani, M., Arteta, J., Benedictow, A., Bergström, R., Bolignano, A., Camps, P., Carvalho, A. C., Christensen, J. H., Couvidat, F., D'Elia, I., van der Gon, H., Descombes, G., Douros, J., Fagerli, H., Fatahi, Y., Friese, E., Frohn, L., Gauss, M., Geels, C., Hänninen, R., Hansen, K., Jorba, O., Kaminski, J. W., Kouznetsov, R., Kranenburg, R., Kuenen, J., Lannuque, V., Meleux, F., Ny\'{\i}ri, A., Palamarchuk, Y., Pérez Garc\'{\i}a-Pando, C., Robertson, L., Russo, F., Segers, A., Sofiev, M., Struzewska, J., Timmermans, R., Uppstu, A., Valdebenito, A., and Ye, Z.: Technical Note: Sensitivity of the CAMS Regional Air Quality Modelling System to Anthropogenic Emission Temporal Variability, Atmos. Chem. Phys., 25, 13245–13278, https://doi.org/10.5194/acp-25-13245-2025, 2025.

Holtslag, A. A. M., Svensson, G., Baas, P., Basu, S., Beare, B., Beljaars, A. C. M., Bosveld, F. C., Cuxart, J., Lindvall, J., Steeneveld, G. J., Tjernström, M., and Van De Wiel, B. J. H.: Stable Atmospheric Boundary Layers and Diurnal Cycles: Challenges for Weather and Climate Models, Bull. Am. Meteorol. Soc., 94, 1691–1706, https://doi.org/https://doi.org/10.1175/BAMS-D-11-00187.1, 2013.

Jo, D. S., Emmons, L. K., Callaghan, P., Tilmes, S., Woo, J.-H., Kim, Y., Kim, J., Granier, C., Soulié, A., Doumbia, T., Darras, S., Buchholz, R. R., Simpson, I. J., Blake, D. R., Wisthaler, A., Schroeder, J. R., Fried, A., and Kanaya, Y.: Comparison of Urban Air Quality Simulations During the KORUS-AQ Campaign With Regionally Refined Versus Global Uniform Grids in the Multi-Scale Infrastructure for Chemistry and Aerosols (MUSICA) Version 0, J. Adv. Model. Earth Syst., 15, e2022MS003458, https://doi.org/https://doi.org/10.1029/2022MS003458, 2023.

Keller, C. A., Long, M. S., Yantosca, R. M., Da Silva, A. M., Pawson, S., and Jacob, D. J.: HEMCO v1.0: A Versatile, ESMF-compliant Component for Calculating Emissions in Atmospheric Models, Geosci. Model Dev., 7, 1409–1417, https://doi.org/10.5194/gmd-7-1409-2014, 2014.

Kleinman, L. I.: Low and High $NO_x$ Tropospheric Photochemistry, J. Geophys. Res., 99, 831–838, https://doi.org/10.1029/94jd01028, 1994.

Kleinman, L. I.: The dependence of tropospheric ozone production rate on ozone precursors, Atmos. Environ., 39, 575–586, https://doi.org/10.1016/j.atmosenv.2004.08.047, 2005.

Krol, M., Houweling, S., Bregman, B., van den Broek, M., Segers, A., van Velthoven, P., Peters, W., Dentener, F., and Bergamaschi, P.: The Two-Way Nested Global Chemistry-Transport Zoom Model TM5: Algorithm and Applications, Atmos. Chem. Phys., 5, 417–432, https://doi.org/10.5194/acp-5-417-2005, 2005.

Lamsal, L. N., Martin, R. V, Padmanabhan, A., van Donkelaar, A., Zhang, Q., Sioris, C. E., Chance, K., Kurosu, T. P., and Newchurch, M. J.: Application of Satellite Observations for Timely Updates to Global Anthropogenic $NO_x$ Emission Inventories, Geophys. Res. Lett., 38, https://doi.org/https://doi.org/10.1029/2010GL046476, 2011.

Lamsal, L. N., Krotkov, N. A., Celarier, E. A., Swartz, W. H., Pickering, K. E., Bucsela, E. J., Gleason, J. F., Martin, R. V., Philip, S., Irie, H., Cede, A., Herman, J., Weinheimer, A., Szykman, J. J., and Knepp, T. N.: Evaluation of OMI Operational Standard $NO_2$ Column Retrievals Using in Situ and Surface-Based $NO_2$ Observations, Atmos. Chem. Phys., 14, 11587–11609, https://doi.org/10.5194/acp-14-11587-2014, 2014.

Lange, K., Richter, A., Schönhardt, A., Meier, A. C., Bösch, T., Seyler, A., Krause, K., Behrens, L. K., Wittrock, F., Merlaud, A., Tack, F., Fayt, C., Friedrich, M. M., Dimitropoulou, E., Van Roozendael, M., Kumar, V., Donner, S., Dörner, S., Lauster, B., Razi, M., Borger, C., Uhlmannsiek, K., Wagner, T., Ruhtz, T., Eskes, H., Bohn, B., Santana Diaz, D., Abuhassan, N., Schüttemeyer, D., and Burrows, J. P.: Validation of Sentinel-5P TROPOMI Tropospheric $NO_2$ Products by Comparison With $NO_2$ Measurements from Airborne Imaging DOAS, Ground-Based Stationary DOAS, and Mobile Car DOAS Measurements During the S5P-VAL-DE-Ruhr Campaign, Atmos. Meas. Tech., 16, 1357–1389, https://doi.org/10.5194/amt-16-1357-2023, 2023.

Lawrence, D. M., Fisher, R. A., Koven, C. D., Oleson, K. W., Swenson, S. C., Bonan, G., Collier, N., Ghimire, B., van Kampenhout, L., Kennedy, D., Kluzek, E., Lawrence, P. J., Li, F., Li, H., Lombardozzi, D., Riley, W. J., Sacks, W. J., Shi, M., Vertenstein, M., Wieder, W. R., Xu, C., Ali, A. A., Badger, A. M., Bisht, G., van den Broeke, M., Brunke, M. A., Burns, S. P., Buzan, J., Clark, M., Craig, A., Dahlin, K., Drewniak, B., Fisher, J. B., Flanner, M., Fox, A. M., Gentine, P., Hoffman, F., Keppel-Aleks, G., Knox, R., Kumar, S., Lenaerts, J., Leung, L. R., Lipscomb, W. H., Lu, Y., Pandey, A., Pelletier, J. D., Perket, J., Randerson, J. T., Ricciuto, D. M., Sanderson, B. M., Slater, A., Subin, Z. M., Tang, J., Thomas, R. Q., Val Martin, M., and Zeng, X.: The Community Land Model Version 5: Description of New Features, Benchmarking, and Impact of Forcing Uncertainty, J. Adv. Model. Earth Syst., 11, 4245–4287, https://doi.org/https://doi.org/10.1029/2018MS001583, 2019.

Lin, H., Jacob, D. J., Lundgren, E. W., Sulprizio, M. P., Keller, C. A., Fritz, T. M., Eastham, S. D., Emmons, L. K., Campbell, P. C., Baker, B., Saylor, R. D., and Montuoro, R.: Harmonized Emissions Component (HEMCO) 3.0 as a Versatile Emissions Component for Atmospheric Models: Application in the GEOS-Chem, NASA GEOS, WRF-GC, CESM2, NOAA GEFS-Aerosol, and NOAA UFS Models, Geosci. Model Dev., 14, 5487–5506, https://doi.org/10.5194/gmd-14-5487-2021, 2021.

Makar, P. A., Staebler, R. M., Akingunola, A., Zhang, J., McLinden, C., Kharol, S. K., Pabla, B., Cheung, P., and Zheng, Q.: The Effects of Forest Canopy Shading and Turbulence on Boundary Layer Ozone, Nat. Commun., 8, 15243, https://doi.org/10.1038/ncomms15243, 2017.

Martin, R. V, Jacob, D. J., Chance, K., Kurosu, T. P., Palmer, P. I., and Evans, M. J.: Global Inventory of Nitrogen Oxide Emissions Constrained by Space-Based Observations of $NO_2$ Columns, Journal of Geophysical Research: Atmospheres, 108, https://doi.org/https://doi.org/10.1029/2003JD003453, 2003.

Martin, V. M., Heald, C. L., and Arnold, S. R.: Coupling Dry Deposition to Vegetation Phenology in the Community Earth System Model: Implications for the Simulation of Surface $O_3$, Geophys. Res. Lett., 41, 2988–2996, https://doi.org/https://doi.org/10.1002/2014GL059651, 2014.

Mazzuca, G. M., Ren, X., Loughner, C. P., Estes, M., Crawford, J. H., Pickering, K. E., Weinheimer, A. J., and Dickerson, R. R.: Ozone Production and Its Sensitivity to $NO_x$ and VOCs: Results From the Discover-AQ Field Experiment, Houston 2013, Atmos. Chem. Phys., 16, 14463–14474, https://doi.org/10.5194/acp-16-14463-2016, 2016.

McDuffie, E. E., Smith, S. J., O'Rourke, P., Tibrewal, K., Venkataraman, C., Marais, E. A., Zheng, B., Crippa, M., Brauer, M., and Martin, R. V: A Global Anthropogenic Emission Inventory of Atmospheric Pollutants From Sector- And

Fuel-Specific Sources (1970–2017): An Application of The Community Emissions Data System (CEDS), Earth Syst. Sci. Data, 12, 3413–3442, https://doi.org/10.5194/essd-12-3413-2020, 2020.

Meinshausen, M., Vogel, E., Nauels, A., Lorbacher, K., Meinshausen, N., Etheridge, D. M., Fraser, P. J., Montzka, S. A., Rayner, P. J., Trudinger, C. M., Krummel, P. B., Beyerle, U., Canadell, J. G., Daniel, J. S., Enting, I. G., Law, R. M., Lunder, C. R., O'Doherty, S., Prinn, R. G., Reimann, S., Rubino, M., Velders, G. J. M., Vollmer, M. K., Wang, R. H. J., and Weiss, R.: Historical Greenhouse Gas Concentrations for Climate Modelling (CMIP6), Geosci. Model Dev., 10, 2057–2116, https://doi.org/10.5194/gmd-10-2057-2017, 2017.

Menut, L., Goussebaile, A., Bessagnet, B., Khvorostiyanov, D., and Ung, A.: Impact of Realistic Hourly Emissions Profiles on Air Pollutants Concentrations Modelled With CHIMERE, Atmos. Environ., 49, 233–244, https://doi.org/https://doi.org/10.1016/j.atmosenv.2011.11.057, 2012.

Miyazaki, K. and Eskes, H.: Constraints on Surface $NO_x$ Emissions by Assimilating Satellite Observations of Multiple Species, Geophys. Res. Lett., 40, 4745–4750, https://doi.org/https://doi.org/10.1002/grl.50894, 2013.

Montzka, S., Aydin, M., Battle, M., Butler, J., Saltzman, E., Hall, B., Clarke, A., Mondeel, D., and Elkins, J.: A 350-Year Atmospheric History for Carbonyl Sulfide Inferred From Antarctic Firn Air and Air Trapped in Ice, J. Geophys. Res., 109, https://doi.org/10.1029/2004JD004686, 2004.

Myriokefalitakis, S., Daskalakis, N., Gkouvousis, A., Hilboll, A., van Noije, T., Williams, J. E., Le Sager, P., Huijnen, V., Houweling, S., Bergman, T., Nüß, J. R., Vrekoussis, M., Kanakidou, M., and Krol, M. C.: Description and Evaluation of a Detailed Gas-Phase Chemistry Scheme in The TM5-MP Global Chemistry Transport Model (r112), Geosci. Model Dev., 13, 5507–5548, https://doi.org/10.5194/gmd-13-5507-2020, 2020.

Naeger, A. R., Newchurch, M. J., Moore, T., Chance, K., Liu, X., Alexander, S., Murphy, K., and Wang, B.: Revolutionary Air-Pollution Applications from Future Tropospheric Emissions: Monitoring of Pollution (TEMPO) Observations, Bull. Am. Meteorol. Soc., 102, E1735–E1741, https://doi.org/https://doi.org/10.1175/BAMS-D-21-0050.1, 2021.

National Center for Atmospheric Research (NCAR): Regridding Meteorological Data, available at: https://github.com/NCAR/IPT/tree/master/Meterological_Reanalysis_Data, last access: 26 January 2022a.

National Center for Atmospheric Research (NCAR): Regridding Emissions, available at: https://ncar.github.io/CAM-chem/examples/functions/Regridding.html, last access: 26 January 2022b.

Park, J., Hong, H., Lee, H., Kim, S.-W., Kim, J., Van Roozendael, M., Fayt, C., Ahn, M.-H., Jacob, D. J., Seo, S., Kim, K.-M., Kim, D., Choi, W., Lee, W.-J., Lee, D.-W., Wagner, T., Richter, A., Krotkov, N. A., Lamsal, L. N., Ko, D. H., Lee, S. H., and Woo, J.-H.: Tropospheric Nitrogen Dioxide Levels Vary Diurnally in Asian Cities, Commun. Earth Environ., 6, 389, https://doi.org/10.1038/s43247-025-02272-7, 2025.

Pfister, G. G., Eastham, S. D., Arellano, A. F., Aumont, B., Barsanti, K. C., Barth, M. C., Conley, A., Davis, N. A., Emmons, L. K., Fast, J. D., Fiore, A. M., Gaubert, B., Goldhaber, S., Granier, C., Grell, G. A., Guevara, M., Henze, D. K., Hodzic, A., Liu, X., Marsh, D. R., Orlando, J. J., Plane, J. M. C., Polvani, L. M., Rosenlof, K. H., Steiner, A. L., Jacob, D. J., and Brasseur, G. P.: The multi-scale infrastructure for chemistry and aerosols (MUSICA), Bull. Am. Meteorol. Soc., 101, E1743–E1760, https://doi.org/10.1175/BAMS-D-19-0331.1, 2020.

Racherla, P. N. and Adams, P. J.: The Response of Surface Ozone to Climate Change Over the Eastern United States, Atmos. Chem. Phys., 8, 871–885, https://doi.org/10.5194/acp-8-871-2008, 2008.

Schwantes, R. H., Emmons, L. K., Orlando, J. J., Barth, M. C., Tyndall, G. S., Hall, S. R., Ullmann, K., St. Clair, J. M., Blake, D. R., Wisthaler, A., and Bui, T. P. V: Comprehensive Isoprene and Terpene Gas-Phase Chemistry Improves Simulated Surface Ozone in the Southeastern US, Atmos. Chem. Phys., 20, 3739–3776, https://doi.org/10.5194/acp-20-3739-2020, 2020.

Schwantes, R. H., Lacey, F. G., Tilmes, S., Emmons, L. K., Lauritzen, P. H., Walters, S., Callaghan, P., Zarzycki, C. M., Barth, M. C., Jo, D. S., Bacmeister, J. T., Neale, R. B., Vitt, F., Kluzek, E., Roozitalab, B., Hall, S. R., Ullmann, K., Warneke, C., Peischl, J., Pollack, I. B., Flocke, F., Wolfe, G. M., Hanisco, T. F., Keutsch, F. N., Kaiser, J., Bui, T. P. V, Jimenez, J. L., Campuzano-Jost, P., Apel, E. C., Hornbrook, R. S., Hills, A. J., Yuan, B., and Wisthaler, A.: Evaluating the Impact of Chemical Complexity and Horizontal Resolution on Tropospheric Ozone Over the Conterminous US With a Global Variable Resolution Chemistry Model, J. Adv. Model. Earth Syst., 14, e2021MS002889, https://doi.org/https://doi.org/10.1029/2021MS002889, 2022.

Sebol, A. E., Canty, T. P., Wolfe, G. M., Hannun, R., Ring, A. M., and Ren, X.: Exploring Ozone Production Sensitivity to $NO_2$ and VOCs in the New York City Airshed in the Spring and Summers of 2017–2019, Atmos. Environ., 324, 120417, https://doi.org/https://doi.org/10.1016/j.atmosenv.2024.120417, 2024.

Shah, V., Jacob, D. J., Dang, R., Lamsal, L. N., Strode, S. A., Steenrod, S. D., Boersma, K. F., Eastham, S. D., Fritz, T. M., Thompson, C., Peischl, J., Bourgeois, I., Pollack, I. B., Nault, B. A., Cohen, R. C., Campuzano-Jost, P., Jimenez, J. L., Andersen, S. T., Carpenter, L. J., Sherwen, T., and Evans, M. J.: Nitrogen Oxides in the Free Troposphere: Implications for Tropospheric Oxidants and the Interpretation of Satellite $NO_2$ Measurements, Atmos. Chem. Phys., 23, 1227–1257, https://doi.org/10.5194/acp-23-1227-2023, 2023.

Shen, Y., Jiang, F., Feng, S., Xia, Z., Zheng, Y., Lyu, X., Zhang, L., and Lou, C.: Increased Diurnal Difference of $NO_2$ Concentrations and Its Impact on Recent Ozone Pollution in Eastern China in Summer, Science of The Total Environment, 858, 159767, https://doi.org/https://doi.org/10.1016/j.scitotenv.2022.159767, 2023.

Sillman, S.: Tropospheric Ozone and Photochemical Smog, Treatise on Geochemistry, 9–9, 407–431, https://doi.org/10.1016/B0-08-043751-6/09053-8, 2003.

Sillman, S. and He, D.: Some theoretical results concerning O3-NOx-VOC chemistry and NOx-VOC indicators, Journal of Geophysical Research: Atmospheres, 107, ACH 26-1-ACH 26-15, https://doi.org/https://doi.org/10.1029/2001JD001123, 2002.

Silvern, R. F., Jacob, D. J., Travis, K. R., Sherwen, T., Evans, M. J., Cohen, R. C., Laughner, J. L., Hall, S. R., Ullmann, K., Crounse, J. D., Wennberg, P. O., Peischl, J., and Pollack, I. B.: Observed $NO/NO_2$ Ratios in the Upper Troposphere Imply Errors in $NO\text{-}NO_2\text{-}O_3$ Cycling Kinetics or an Unaccounted $NO_x$ Reservoir, Geophys. Res. Lett., 45, 4466–4474, https://doi.org/https://doi.org/10.1029/2018GL077728, 2018.

Silvern, R. F., Jacob, D. J., Mickley, L. J., Sulprizio, M. P., Travis, K. R., Marais, E. A., Cohen, R. C., Laughner, J. L., Choi, S., Joiner, J., and Lamsal, L. N.: Using Satellite Observations of Tropospheric $NO_2$ Columns to Infer Long-Term Trends in US $NO_x$ Emissions:~The Importance of Accounting for the Free Tropospheric $NO_2$ Background, Atmos. Chem. Phys., 19, 8863–8878, https://doi.org/10.5194/acp-19-8863-2019, 2019.

Soulie, A., Granier, C., Darras, S., Zilbermann, N., Doumbia, T., Guevara, M., Jalkanen, J.-P., Keita, S., Liousse, C., Crippa, M., Guizzardi, D., Hoesly, R., and Smith, S.: Global Anthropogenic Emissions (CAMS-GLOB-ANT) for the Copernicus Atmosphere Monitoring Service Simulations of Air Quality Forecasts and Reanalyses, Earth System Science Data Discussions, 2023, 1–45, https://doi.org/10.5194/essd-2023-306, 2023.

Stjern, C. W., Hodnebrog, Ø., Myhre, G., and Pisso, I.: The Turbulent Future Brings a Breath of Fresh Air, Nat. Commun., 14, 3735, https://doi.org/10.1038/s41467-023-39298-4, 2023.

Strosnider, H. M., Chang, H. H., Darrow, L. A., Liu, Y., Vaidyanathan, A., and Strickland, M. J.: Age-specific associations of ozone and fine particulate matter with respiratory emergency department visits in the United States, Am. J. Respir. Crit. Care Med., 199, 882–890, https://doi.org/10.1164/rccm.201806-1147OC, 2019.

Tang, W., Emmons, L. K., Buchholz, R. R., Wiedinmyer, C., Schwantes, R. H., He, C., Kumar, R., Pfister, G. G., Worden, H. M., Hornbrook, R. S., Apel, E. C., Tilmes, S., Gaubert, B., Martinez-Alonso, S.-E., Lacey, F., Holmes, C. D., Diskin, G. S., Bourgeois, I., Peischl, J., Ryerson, T. B., Hair, J. W., Weinheimer, A. J., Montzka, D. D., Tyndall, G. S., and Campos, T. L.: Effects of Fire Diurnal Variation and Plume Rise on U.S. Air Quality During FIREX-AQ and WE-CAN Based on the Multi-Scale Infrastructure for Chemistry and Aerosols (MUSICAv0), Journal of Geophysical Research: Atmospheres, 127, e2022JD036650, https://doi.org/https://doi.org/10.1029/2022JD036650, 2022.

Tang, W., Emmons, L. K., Worden, H. M., Kumar, R., He, C., Gaubert, B., Zheng, Z., Tilmes, S., Buchholz, R. R., Martinez-Alonso, S.-E., Granier, C., Soulie, A., McKain, K., Daube, B. C., Peischl, J., Thompson, C., and Levelt, P.: Application of the Multi-Scale Infrastructure for Chemistry and Aerosols Version 0 (MUSICAV0) for Air Quality Research in Africa, Geosci. Model Dev., 16, 6001–6028, https://doi.org/10.5194/gmd-16-6001-2023, 2023a.

Tang, W., Pfister, G. G., Kumar, R., Barth, M., Edwards, D. P., Emmons, L. K., and Tilmes, S.: Capturing High-Resolution Air Pollution Features Using the Multi-Scale Infrastructure for Chemistry and Aerosols Version 0 (MUSICAv0) Global Modeling System, Journal of Geophysical Research: Atmospheres, 128, e2022JD038345, https://doi.org/https://doi.org/10.1029/2022JD038345, 2023b.

Tang, W., Emmons, L. K., Wiedinmyer, C., Partha, D. B., Huang, Y., He, C., Zhang, J., Barsanti, K. C., Gaubert, B., Jo, D. S., Zhang, J., Buchholz, R., Tilmes, S., Vitt, F., Granier, C., Worden, H. M., and Levelt, P. F.: Disproportionately

Large Impacts of Wildland-Urban Interface Fire Emissions on Global Air Quality and Human Health, Sci. Adv., 11, eadr2616, https://doi.org/10.1126/sciadv.adr2616, 2025.

Tao, M., Fiore, A. M., Jin, X., Schiferl, L. D., Commane, R., Judd, L. M., Janz, S., Sullivan, J. T., Miller, P. J., Karambelas, A., Davis, S., Tzortziou, M., Valin, L., Whitehill, A., Civerolo, K., and Tian, Y.: Investigating Changes in Ozone Formation Chemistry during Summertime Pollution Events over the Northeastern United States, Environ. Sci. Technol., 56, 15312–15327, https://doi.org/10.1021/acs.est.2c02972, 2022.

Tao, M., Fiore, A. M., Karambelas, A., Miller, P. J., Valin, L. C., Judd, L. M., Tzortziou, M., Whitehill, A., Teora, A., Tian, Y., Civerolo, K. L., Tong, D., Ma, S., Adamo, S. B., and Holloway, T.: Insights Into Summertime Surface Ozone Formation From Diurnal Variations in Formaldehyde and Nitrogen Dioxide Along a Transect Through New York City, Journal of Geophysical Research: Atmospheres, 130, e2024JD040922, https://doi.org/https://doi.org/10.1029/2024JD040922, 2025.

Tilmes, S., Hodzic, A., Emmons, L. K., Mills, M. J., Gettelman, A., Kinnison, D. E., Park, M., Lamarque, J.-F., Vitt, F., Shrivastava, M., Campuzano-Jost, P., Jimenez, J. L., and Liu, X.: Climate Forcing and Trends of Organic Aerosols in the Community Earth System Model (CESM2), J. Adv. Model. Earth Syst., 11, 4323–4351, https://doi.org/https://doi.org/10.1029/2019MS001827, 2019.

Tonnesen, G. S. and Dennis, R. L.: Analysis of Radical Propagation Efficiency to Assess Ozone Sensitivity to Hydrocarbons and $NO_x$ 1. Local Indicators of Instantaneous Odd Oxygen Production Sensitivity, Journal of Geophysical Research Atmospheres, 105, 9213–9225, https://doi.org/10.1029/1999JD900371, 2000.

Travis, K. R., Jacob, D. J., Fisher, J. A., Kim, P. S., Marais, E. A., Zhu, L., Yu, K., Miller, C. C., Yantosca, R. M., Sulprizio, M. P., Thompson, A. M., Wennberg, P. O., Crounse, J. D., St. Clair, J. M., Cohen, R. C., Laughner, J. L., Dibb, J. E., Hall, S. R., Ullmann, K., Wolfe, G. M., Pollack, I. B., Peischl, J., Neuman, J. A., and Zhou, X.: Why do Models Overestimate Surface Ozone in the Southeastern United States?, Atmos. Chem. Phys., 16, 13561–13577, https://doi.org/10.5194/acp-16-13561-2016, 2016.

U.S. Environmental Protection Agency (EPA): 2017 National Emissions Inventory (NEI) Data, available at: https://www.epa.gov/air-emissions-inventories/2017-national-emissions-inventory-nei-data, last access: 25 January 2022.

U.S. Environmental Protection Agency (EPA): Air Quality System (AQS) Pre-generated Data Files, available at: https://aqs.epa.gov/aqsweb/airdata/download_files.html, last access: August 2023.

U.S. Environmental Protection Agency (EPA): Hazardous Air Pollutants, available at: https://www.epa.gov/haps, last access: 23 January 2024.

Wang, J. X. L. and Angell, J. K.: Air Stagnation Climatology for the United States (1948-1998), 1999.

Wang, Y. X., McElroy, M. B., Jacob, D. J., and Yantosca, R. M.: A Nested Grid Formulation for Chemical Transport Over Asia: Applications to CO, Journal of Geophysical Research: Atmospheres, 109, https://doi.org/https://doi.org/10.1029/2004JD005237, 2004.

Wiedinmyer, C., Kimura, Y., McDonald-Buller, E. C., Emmons, L. K., Buchholz, R. R., Tang, W., Seto, K., Joseph, M. B., Barsanti, K. C., Carlton, A. G., and Yokelson, R.: The Fire Inventory From NCAR Version 2.5: An Updated Global Fire Emissions Model for Climate and Chemistry Applications, EGUsphere, 2023, 1–45, https://doi.org/10.5194/egusphere-2023-124, 2023.

Williams, J. E., Boersma, K. F., Le Sager, P., and Verstraeten, W. W.: The High-Resolution Version of TM5-MP for Optimized Satellite Retrievals: Description and Validation, Geosci. Model Dev., 10, 721–750, https://doi.org/10.5194/gmd-10-721-2017, 2017.

Wu, Y., Zhao, K., Ren, X., Dickerson, R. R., Huang, J., Schwab, M. J., Stratton, P. R., Daley, H., Li, D., and Moshary, F.: Ozone Pollution Episodes and PBL Height Variation in the NYC Urban and Coastal Areas During LISTOS 2019, Atmos. Environ., 320, 120317, https://doi.org/https://doi.org/10.1016/j.atmosenv.2023.120317, 2024.

Yang, L. H., Jacob, D. J., Dang, R., Oak, Y. J., Lin, H., Kim, J., Zhai, S., Colombi, N. K., Pendergrass, D. C., Beaudry, E., Shah, V., Feng, X., Yantosca, R. M., Chong, H., Park, J., Lee, H., Lee, W.-J., Kim, S., Kim, E., Travis, K. R., Crawford, J. H., and Liao, H.: Interpreting Gems Geostationary Satellite Observations of the Diurnal Variation of Nitrogen Dioxide ($NO_2$) Over East Asia, EGUsphere, 2023, 1–25, https://doi.org/10.5194/egusphere-2023-2979, 2023.

Yu, K., Jacob, D. J., Fisher, J. A., Kim, P. S., Marais, E. A., Miller, C. C., Travis, K. R., Zhu, L., Yantosca, R. M., Sulprizio, M. P., Cohen, R. C., Dibb, J. E., Fried, A., Mikoviny, T., Ryerson, T. B., Wennberg, P. O., and Wisthaler, A.: Sensitivity to Grid Resolution in the Ability of a Chemical Transport Model to Simulate Observed Oxidant Chemistry Under High-Isoprene Conditions, Atmos. Chem. Phys., 16, 4369–4378, https://doi.org/10.5194/acp-16-4369-2016, 2016.

Zoogman, P., Liu, X., Suleiman, R. M., Pennington, W. F., Flittner, D. E., Al-Saadi, J. A., Hilton, B. B., Nicks, D. K., Newchurch, M. J., Carr, J. L., Janz, S. J., Andraschko, M. R., Arola, A., Baker, B. D., Canova, B. P., Chan Miller, C., Cohen, R. C., Davis, J. E., Dussault, M. E., Edwards, D. P., Fishman, J., Ghulam, A., González Abad, G., Grutter, M., Herman, J. R., Houck, J., Jacob, D. J., Joiner, J., Kerridge, B. J., Kim, J., Krotkov, N. A., Lamsal, L., Li, C., Lindfors, A., Martin, R. V, McElroy, C. T., McLinden, C., Natraj, V., Neil, D. O., Nowlan, C. R., O′Sullivan, E. J., Palmer, P. I., Pierce, R. B., Pippin, M. R., Saiz-Lopez, A., Spurr, R. J. D., Szykman, J. J., Torres, O., Veefkind, J. P., Veihelmann, B., Wang, H., Wang, J., and Chance, K.: Tropospheric emissions: Monitoring of pollution (TEMPO), J. Quant. Spectrosc. Radiat. Transf., 186, 17–39, https://doi.org/https://doi.org/10.1016/j.jqsrt.2016.05.008, 2017.